Title
Effects of in situ Surface Layer Heating on Laser Powder Bed Fusion of 316L Stainless Steel

Permalink
https://escholarship.org/uc/item/9c47s1s7

Author
Smith, William Louis

Publication Date
2021

Peer reviewed|Thesis/dissertation

Effects of in situ Surface Layer Heating on Laser Powder Bed Fusion of 316L Stainless Steel

By

WILLIAM LOUIS SMITH

THESIS

Submitted in partial satisfaction of the requirements for the degree of

MASTER OF SCIENCE

in

Mechanical and Aerospace Engineering

in the

OFFICE OF GRADUATE STUDIES

of the

UNIVERSITY OF CALIFORNIA

DAVIS

Approved:

———————————————————

Micheal R. Hill, Chair

———————————————————

Jeffery C. Gibeling

———————————————————

Manyalibo J. Matthews

Committee in Charge

2021

Abstract

Additively manufacturing metal parts through laser powder bed fusion (LPBF) is of growing interest to many fields, ranging from medical to aerospace. Typical LPBF systems use a single laser to weld the metal powder, which leads to sharp temperature gradients as metal rapidly melts and solidifies. However, due to the extreme heating and cooling cycles experienced during LPBF, the resulting parts are often plagued with internal residual stresses which can cause warping and a deviation from the original design specifications. This work explores an in situ method of mitigating residual stress by using a dual laser system where a secondary diode laser projects uniformly over a large area to heat the current top layer. With the ability to determine the timing, duration, intensity, and periodicity of the secondary laser projection, the user is allowed full control of the thermal history of their part throughout the build. This selective heating of the welded surface pattern reduces the temperature gradient between layers, thus reducing the residual stress. The capability to control grain growth in LPBF using the secondary surface-heating laser is also explored in this work. Such a system allows the user to control the solidification time, thus controlling the transition through various phases and ultimately the resulting microstructure. This secondary surface heating source provides an alternative to other heat treatment methods such as post annealing and build plate heating. Directly heating the topmost layer allows for temperature control within the region most affected by the welding.

Acknowledgments

Well, this has certainly been a much longer journey than I expected. There have been quite a few hurdles along the way including hospital stays, lab changes, and even a global pandemic, but I have finally reached the finish line despite it all.

Firstly, I have to thank Professor Mike Hill for agreeing to be my advisor and for guiding me along this journey all these years. You've been a reliable source of information whenever I had questions about experiments and I believe that going through the writing process with you has made me a much better writer. Thank you to Professor Gibeling for agreeing to take time out of your busy schedule to review this work. I'd also like to thank Ibo Matthews for taking me under your wing as my resident LLNL advisor and agreeing to support me throughout this degree program. It really appreciate you providing me with the opportunity to break into the metal AM space via your project and I look forward to working with you in the future.

None of this work would have been possible if it weren't for the support I received from LLNL. To everyone at LLNL, from the administrative staff who handled the funding of my tuition to the machinists who prepared my samples, I really appreciate all of the assistence I've recieved from you over the years. I'd like to thank Rishi and Ava for providing the modeling data and I'd also like to thank Maria, Bjørn, and Don for assisting with the neutron diffraction experiments at LANL. The results from each of your contributions has added so much value to this thesis. I'd like to give a special thanks to Gabe Guss, a.k.a. our resident LabVIEW angel. I don't know how you do what you do, but I do know that none of our printers would run if we didn't have you around to program them. And I would be

remissed if I didn't thank John Roehling for being my partner in crime since the very start of my experiments. I couldn't possibly recount all the ways in which you've helped me over the years, but suffice to say I couldn't have asked for a better lab mate.

Lastly, I have to thank my parents. With each passing year, I appreciate more and more just how fortunate I am to have been raised and supported by a family that never set limits on my life and, for that, I am eternally grateful.

Contents

List of Tables

List of Figures

1 Introduction

Additive manufacturing (AM) is an ever-growing method of fabricating complex products for commercial use, typically requiring fewer fabrication steps than traditional manufacturing [2]. Due to this high level of interest in metal AM within the industrial space, there is a need to improve upon the metal AM printing process. It is not uncommon for there to be macroscopic part-to-part variability present within additively manufactured parts, which can give rise to print failures and catastrophic defects that greatly reduce part service life or even prevent successful completion of the build altogether [3]. These inconsistencies have motivated the commercialization of layer-by-layer in situ process monitoring within AM, especially for the laser powder bed fusion (LPBF) process [4].

One of the major concerns for parts made using the LPBF process, and the focus of this work, is the formation of residual stress. Due to the repeated welding performed during LPBF, which consists of rapid heating and cooling cycles at rates up to $\approx 10^6$ K/s [5], printed parts are subject to high temperature gradients which can produce large residual stresses [6]. These residual stresses can lead to a wide range of macroscopic defects including warping, cracking, and even delamination from the build plate, which all contribute to lowering the print consistency of LPBF machines [7, 8, 9, 10]. Given that post-build annealing would not affect this high potential for print failure, having the ability to reduce residual stresses induced during LPBF in situ is very appealing.

Given that large stresses are typical within welds used to conjoin multiple pieces of material, it follows that LPBF parts will have large residual stresses since the entire part is formed through a repeated welding process [11]. The high temperature gradients inherent

1

to this welding process lead to non-uniform thermal expansions which cause localized plastic yielding (deformation) of the metal. As the metal affected by the melting laser is being heated, it expands and softens, lowering its yield strength. The expansion of this softer metal is constrained by the surrounding cooler and stronger (higher yield strength) metal, causing plastic deformation of the soft material, and generating compressive strain. This hot and plastically compressed material begins to contract as it cools, but this contraction is constrained by the still stronger and cooler surrounding material. This constrained contraction converts the stresses within the recently welded material from compressive to tensile, which in turn is balanced out by compressive stresses in the cooler material [11, 12].

In an ideal situation, a material could be produced without any residual stresses by ensuring that there were no deformation gradients present at any point during its formation. In practice however, the best way to reduce residual stress formation is to minimize the temperature gradients and rapid cooling rates, which can be difficult to accomplish within LPBF due to the small (≈100 micron) spot size of the heating source. Since the residual stress in any given material cannot exceed its yield strength, heating a part up to an annealing temperature and cooling it slowly and uniformly will reduce the internal stresses to a level below the yield strength of the material (at the annealing temperature) [13]. This is traditionally performed by annealing samples in a furnace after printing, which leads to additional processing time and can alter the as-built microstructure. A post-build heat treatment such as this one also does not address any distortions that may have taken place during printing. Logically, many of the simplest and most common methods utilized to reduce residual stress during printing involve secondary heating, which include but are not limited to preheating the build plate during printing, heating the entire build chamber, or annealing the parts in a furnace after printing [10, 14, 15]. Though it was not explored in this work, the scanning strategy can also affect the resulting residual stress based on path length and the scanning speed [7, 11, 12, 16, 17, 18]. Temperature gradients within LPBF are generally known to play a major role in the magnitude of residual stresses. However, it has been shown that

the distribution of the final residual stress state is highly dependent on the solidification shrinkage mechanism dictated by the scanning pattern [19].

Although residual stress cannot be measured directly, there are several available techniques which measure associated properties (such as cutting-induced deformation or atomic spacing) and determine residual stress through data analysis. Among the techniques for determining residual stress are mechanical methods such as hole drilling [20], the slitting method [21, 22], the contour method [23, 24], and the bridge curvature method (BCM) [25]. There are also diffraction-based methods such as neutron diffraction [26] and X-ray diffraction [27, 28], of which the former can allow for characterization of the internal stresses beneath the surface of the sample [10]. Since these residual stress measurement methods rely on very different assumptions and often have systematic errors [29], it can be useful to make measurements with complementary techniques (e.g. a mechanical relaxation method and a diffraction method) and then use the full set of results as part of an engineering analysis [26]. Moreover, the contour method provides a single stress component along a given plane with high spatial resolution (0.05 – 1 mm) in 2D, whereas neutron diffraction provides three stress components for each measurement location, which can be placed at arbitrary locations within the sample, with low spatial resolution in 2D (typically 2 mm).

The majority of this thesis has been previously published as:

- J.D. Roehling, W.L. Smith, T.T. Roehling, B. Vrancken, G.M. Guss, J.T. McKeown, M.R. Hill, M.J. Matthews. Reducing residual stress by selective large-area diode surface heating during laser powder bed fusion additive manufacturing. *Additive Manufacturing*, **28**, 228-235, August 2019, `https://doi.org/10.1016/j.addma.2019.05.009`.

- W.L. Smith, J.D. Smith, M. Strantza, R.K. Ganeriwala, A.S. Ashby, B. Vrancken, B. Clausen, G.M. Guss, D.W. Brown, J.T. McKeown, M.R. Hill, M.J. Matthews. Residual Stress Analysis of in situ Surface Layer Heating Effects on Laser Powder Bed Fusion of 316L Stainless Steel, *Additive Manufacturing*, **47**, November 2021, `https://doi.org/10.1016/j.addma.2021.102252`.

2 Residual Stress Characterization and Experimental Setup

2.1 Residual stress characterization

Residual stress is not a property that can be measured directly, therefore it can only be determined by measuring associated properties and then using those to calculate residual stress at a given location. There are several methods for determining residual stress with varying capabilities and limitations, with spatial resolutions ranging from 10 µm to over 10 mm and penetration depths from 1 m down to less than 1 µm. These include mechanical methods such as hole drilling, the contour method, crack slitting, and the bridge curvature method, which all involve mechanically removing material to measure some sort of displacement. There are also diffraction based methods such as X-ray diffraction and neutron diffraction, which are each non-destructive methods capable of measuring stresses at or beneath the surface of the material. Each of these methods relies on a different set of assumptions in order to make it possible to determine the residual stress, so it can often be advantageous to utilize complementary techniques (e.g. diffraction and destructive) in one study and compare the results in order to validate the outcome.

In this work, three independent stress characterization approaches were carried out: the bridge curvature method (BCM), contour method, and neutron diffraction. The BCM is the simplest of the three stress measurements, and was therefore carried out first for assurance of the effectiveness of the residual stress reduction method. For this method, samples are

printed with two thick legs attached to the build substrate and are connected by a thin overhang at the top of the sample. After printing, the part is sectioned such that only one of the legs is detached from the build plate, relieving internal stresses and allowing the part to deform as a result. Even though stresses are surely relived throughout the entire volume of the sample sample, these bridge samples are designed in such a way that the legs are much thicker than the overhang section, ensuring that the most dramatic stress relaxation within the sample will be confined to the overhang. By performing a height profile scan of the top surface of a bridge, before and after cutting through one of the legs, a radius of curvature can be calculated based on the difference in the height profiles before and after deflection. Applying this to classical beam theory:

$$\sigma = EL\frac{\partial^2 \nu}{\partial x^2} \tag{2.1}$$

the radius of curvature ($\frac{\partial^2 \nu}{\partial x^2}$) can be used to calculate the maximum stress (σ) in the overhang based on the Young's modulus (E) and half the thickness of the overhang (L). While this does not provide an exact value for the stress within each sample, this qualitative approach is a relatively simple method for comparing stresses across a sample set and is certainly useful for gauging the effectiveness of a residual stress reduction.

Unlike the BCM, the contour method [29] provides a spatial distribution of internal residual stresses underneath the surface of the part. To obtain this residual stress distribution, samples are sectioned using wire electrical discharge machining (EDM), which relieves internal stresses along this cut plane and creates two mirror-imaged surfaces. The height profiles of the two cut surfaces are measured to determine the displacements that resulted from stress relieved by the cut, which can be performed using a coordinate measuring machine or a non-contact optical scanner [30]. The profiles of the two cut surfaces are aligned, overlapped, averaged, and smoothed to remove noise. This processed profile data is first inverted about the surface normal and is then used as a displacement boundary condition

applied to the cut surface of a 3-dimensional representation of the sample within finite element method software, forcing it into the deformed condition. The stresses normal to the cut surface resulting from this forced deformation represent the residual stresses present to prior to sectioning [29, 30].

Neutron diffraction is a non-destructive residual stress measurement technique with the ability to measure stresses underneath the surface of the sample. A crystalline material is placed in the path of a beam of neutrons, off of which a diffraction pattern is reflected, revealing information about the lattice spacing within the material. For the purpose of measuring residual stress, the collected diffraction patterns are used to determine the lattice parameters through Rietveld refinement of the full diffraction pattern. The determined lattice parameters are then used to calculate the three orthogonal strain components: longitudinal (ε_{ii}), transverse (ε_{jj}), and build (ε_{kk}) from:

$$\varepsilon_{ii} = \frac{a_{ii} - a_{0,ii}}{a_{0,ii}} \tag{2.2}$$

where a_{ii} is the averaged lattice parameter of the measured sample along direction ii and $a_{0,ii}$ is the stress-free averaged lattice parameter. The lattice parameters of this assumed stress-free sample serve as a reference to which the lattice parameters of all the other printed samples are compared to calculate their strains. The rectangular reference sample is assumed to be free of macro-stresses due to its small size [31].

As discussed by Daymond [32], using the lattice parameter determined from Rietveld refinement ensures that the determined lattice strain is representative of the bulk average strain in the gauge volume, and thus the standard continuum mechanics material parameters (Young's modulus and Poisson's ratio) can be used when calculating the residual stresses from the measured strains. The strains (ε_{ii}) are used to compute stresses (σ_{ii}) based on the

material properties of the samples using Hooke's law:

$$\sigma_{ii} = \frac{E}{(1+\nu)(1-2\nu)}((1-\nu)\varepsilon_{ii} + \nu(\varepsilon_{jj} + \varepsilon_{kk})) \tag{2.3}$$

where ii, jj, and kk represent the directions of each of the three orthogonal stress and strain components, E is the Young's modulus (200 GPa), and ν is the Poisson's ratio (0.3) of 316L stainless steel [33, 34].

2.2 Experimental setup

All samples produced in this study were printed using a small-scale custom LPBF system (Fig. 2.1A,B) originally developed to print metal parts using a wide area projection to flash sinter the metal powder (Matthews, et al. [35]). The current system consists of two primary heat sources, the first being an nLight scanning fiber laser (1078 nm, 1 kW) and the second a set of four Trumpf laser diodes (1000 nm, 1.25 kW each, 5kW total). The four laser diodes are focused into a homogenizer that combines the individual laser profiles into a single beam of light that has near homogeneous spatial intensity as it exits the outlet of the homogenizer. This uniform intensity diode beam is passed through an aluminum mask, which clips and shapes the beam projection into an area that matches the desired layer pattern at the 25.4 mm diameter build plate surface. The diode light (775 W/mm^2 maximum) is then reflected from a dichroic mirror onto a build plate. The focused scanning laser with a 1/e^2 diameter of 80 µm, which is directed by a Nutfield 3XB galvanometer mirror scanner, passes through this same dichroic mirror and is coincident with the diode laser light. The build plate, along with a powder spreader and powder feed system, is housed within a glovebox filled with argon and an O$_2$ level of less than 0.01% (100 ppm, Fig. 2.1C). Custom LabView software is used to control the lasers and powder distribution system.

Rectangular 316L stainless steel specimens were printed in this study with a length and width of approximately 20 mm and 10 mm, respectively. Samples in the initial qualitative
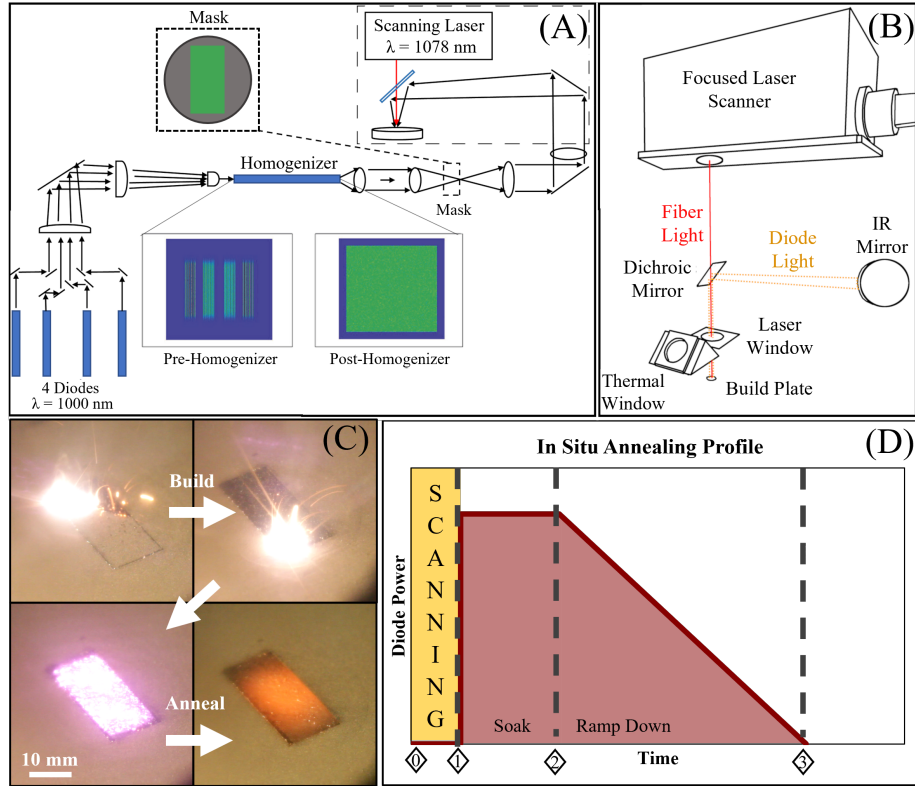
Figure 2.1: (A - B) Schematic of the diode annealing LPBF system. (C) Photos of the layer melting and annealing steps within the glovebox build chamber. (D) An example of a diode annealing power profile. (0) The fiber laser is scanning and melting the loose powder (1) Melting ends and laser diode emission initiates at full power and maintains for the duration of the soak (2) Soaking ends and the diodes ramp down from maximum power to 0 W (3) Annealing is complete.

study consisted of 5 mm tall rectangular bridges and the second study analyzed 10 mm tall rectangular bricks. For all samples (unless noted otherwise), the scanning laser was held at a constant power and speed of 250 W and 278 mm/s, respectively. These parameters were chosen to maximize part density (above 99%, Fig. 2.2) as well as minimize evaporation from the melt pool due to its proximity to the build window. Layers were scanned using a single contour pass around the perimeter and a crosshatch scan strategy where the scanning vectors were angled 45° with respect to the longitudinal axis of the part was rotated 90° between each layer.
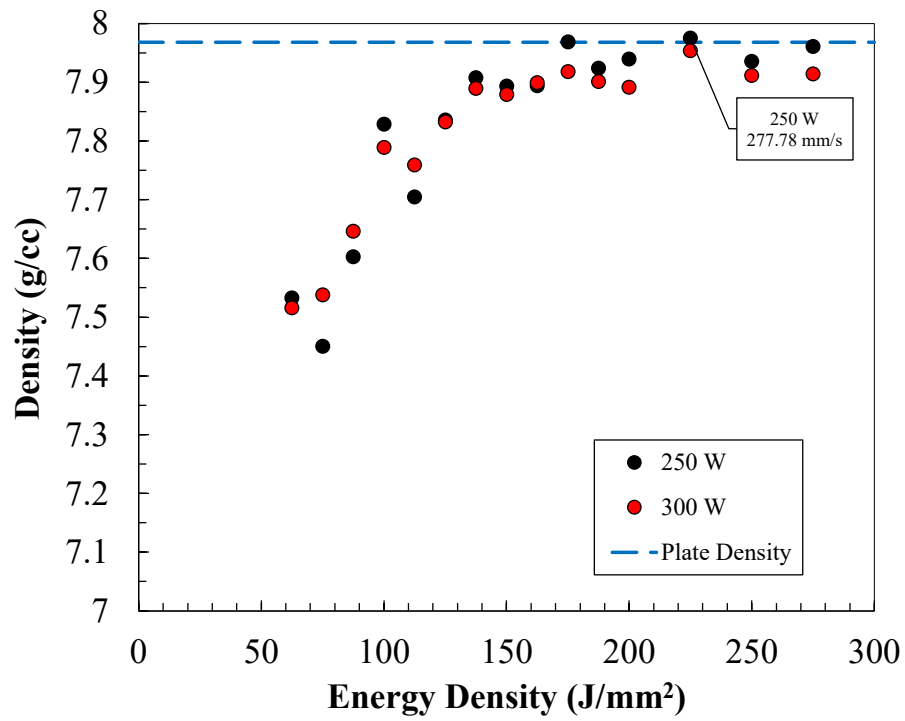
Figure 2.2: Density of 316L stainless steel samples produced using a laser power of 250 W (black) and 300 W (red) for various scanning speeds. The build plate density (blue line) was used as a reference.

3 Effect of *in situ* Annealing on Residual Stress of 316L Stainless Steel - A Qualitative Study

3.1 Introduction

In this chapter, the initial attempts to reduce residual stress using an in situ annealing method during metal AM are outlined. Laser powder bed fusion (LPBF) was used to produce 316L stainless steel bridges and a set of four diode lasers were used to provide secondary heating by illuminating the overhang layers with a uniform intensity projection. By applying this projection immediately after the overhang layers were welded, the time spent at elevated temperatures is increased and allows for slower cooling. Samples were heated to a range of maximum temperatures in order to determine an effective annealing temperature. This in situ annealing method produced parts with residual stress levels comparable to those treated with traditional furnace annealing, greatly reducing the need for post-processing. There was no significant change in microstructure when using this in situ annealing method.

A previous version of this chapter is published in *Additive Manufacturing* as:

- J.D. Roehling, W.L. Smith, T.T. Roehling, B. Vrancken, G.M. Guss, J.T. McKeown, M.R. Hill, M.J. Matthews. Reducing residual stress by selective large-area diode surface heating during laser powder bed fusion additive manufacturing. *Additive Manufacturing*, **28**, 228-235, August 2019, https://doi.org/10.1016/j.addma.2019.05.009.

3.2 Methods

3.2.1 Experimental setup

All bridge samples were built using the standard printing parameters of 50 µm layers with hatches spaced 100 µm apart, which were angled at 45° with respect to the long axis of the bridge. These zigzag scanning laser hatches were rotated 90° between layers and scanned at 278 mm/s with a laser power of 250 W. The bridges were printed with dimensions of 20 mm (L) × 11 mm (W) × 5 mm (H) on build plates that were 25.4 mm (1 in.) in diameter and 6.35 mm (0.25 in.) thick. The 1.5 mm (30 layers) thick overhang section of the bridges had a span of 6 mm between the two legs, which will contribute to the curvature measured to allow for a residual stress comparison. In order to build bridge overhang sections that had acceptable down-facing surface quality, the scanning laser power was lowered and gradually increased over the first five layers of the overhang [36]. Otherwise, the unbound powder underneath the current layer would melt. Using only the scanning laser, the first three layers of the overhang section were built using 80 W and the fourth and fifth layers were build using 170 and 250 W, respectively. Despite heating the thin overhang to high temperatures, the unbound powder adjacent and underneath the bridge was unaffected (no sintering was observed).

For bridge samples that were subject to in situ annealing, the laser diodes illuminated the top surface of the overhang layers immediately after the initial laser scanning was complete (Fig. 3.1). The diode light was imaged from the mask plane onto the recently scanned material such that the adjacent powder was not illuminated, ensuring this powder was not sintered and did not disrupt the building process. The laser diodes were initiated at their designated maximum power and then linearly ramped down to 0 W over 20 seconds. The first five layers of the bridge overhang sections were not subjected to diode annealing to avoid dross formation on the underside of the overhang, but each remaining layer was illuminated

by the laser diodes immediately after being melted by the scanning laser. The diode laser powers used for the in situ annealing of the overhang bridge layers were nominally 400, 800, 1000, and 1200 W (actual power was measured to be 400, 840, 1080, an 1310 W (Table 3.1)). The masks used to block unwanted diode illumination for the support and overhang layers let 25.3% and 37.3% of the diode emission through, respectively.

Samples not subjected to diode heating were annealed traditionally (post-build, in a furnace) to make a benchmark comparison to the in situ annealed bridge samples. This annealing took place in a horizontal tube furnace in an inert (Ar) atmosphere while the bridges were still intact and attached to the build plate. The furnace was brought up to temperature as quickly possible (33 °C/min), held for a specified amount of time, and cooled back down to room temperature over the course of 3 hours.

Table 3.1: Processing parameters for the bridges and their measured annealing temperatures. The final two samples in **bold** were annealed in a tube furnace after printing. Three identical bridge samples were printed for each parameter set.

Diode Laser Power (W)	Maximum Diode Power Density (W/mm^2)	Diode Energy Density (J/mm^2)	Approximate Annealing Temperature (C$^\circ$)
0	0	0	N/A
400	0.68	6.78	350
840	1.42	14.24	625
1080	1.83	18.31	865
1310	2.22	22.21	1015
0	**0**	**0**	**625 (30 min)**
0	**0**	**0**	**1000 (4 min)**

3.2.2 Thermal measurements

A FLIR A6230 thermal camera was used for temperature measurements through a 3-mm thick anti-reflective ZnSe window (Fig. 2.1). This was used to measure both the spatial and time-dependent temperature distribution of the annealing process. The camera used wavelengths between 3 and 5 µm. Since it can only record temperatures using a finite range, two ranges were used: (1) 310 °C – 890 °C, and (2) 630 °C – 1250 °C. The thermal camera was calibrated using a heated 316L stainless steel plate with a type-K thermocouple welded to the surface. The plate was heated with a resistive ceramic heater while the camera
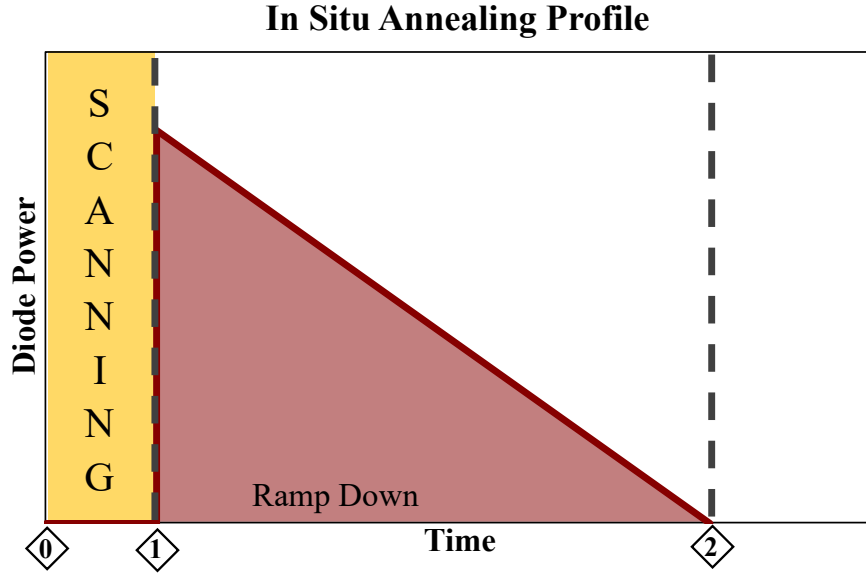
Figure 3.1: An example of a diode annealing power profile. (0) The fiber laser is scanning and welding the loose powder (1) Welding ends and laser diode emission initiates at full power and immediately begins to ramp down to 0 W (2) Annealing is complete.

recorded. Once the plate reached thermal equilibrium at some temperature, the emissivity value was adjusted until the camera and thermocouple readings were in good agreement. This was performed for dozens of temperatures from 300 °C to 1000 °C, such that both ranges described above were calibrated. An approximately linear change in emissivity with temperature was observed, so an effective emissivity of 0.4 was chosen as it layed in the middle of the measured emissivity range. This results in an approximate error in the temperature measurement of 25 °C (conservative estimate).

3.2.3 Characterization

The residual stress of all samples produced in this study was characterized following the bridge curvature method (BCM). This was carried out by measuring the top surface profile of the bridges before and after they were cut using a Keyence VR optical microscope profile scanner. The height was averaged along the width to produce a single curve along the length. An averaged thickness of the overhang was calculated by completely removing the bridges

from the build plate, flipping them over, and measuring the height profile of the underside of the bridges while correcting for the measured top surface. Using this thickness along with the deflection calculated from the difference between the curvature of the bridges before and after cutting, the amount of residual stress released in the overhang section due to cutting was calculated using simple beam theory [11].

After residual stress measurements were complete, samples were sectioned in half along their length using a slow-speed diamond saw. The newly-exposed surface was micropolished and hardness data within the overhang was collected using a Phase II, 900-391 Vickers microhardness tester with a 100 g load and a 15 s dwell time. Measurements were made along the length of the overhang, near the top and bottom.

Electron back-scatter diffraction (EBSD) information was collected on a FEI XL-30 field-emission gun (FEG) scanning electron microscope (SEM) using an EDAX DigiView EBSD camera. Data processing and analysis were performed in EDAX OIM Analysis software. Optical microscope images were collected on an Olympus DSX510 with automatic stitching. Hardness data was collected on a Phase II, 900-391 Vickers microhardness tester using a 100 g (0.981 N) load with a 15 s dwell time. All microstructure data were collected after diamond sectioning, mechanical polishing, and electrolytic etching using 10% oxalic acid at 6 V for 25 s.

3.3   Results

The released residual stresses measured after in situ annealing by the laser diodes are shown in Fig. 3.2A as a function of the diode power density input. These in situ annealing results are compared to two furnace anneal processes (dashed lines). Each data point shown is the average of three separate bridges, with the error bars corresponding to one standard deviation (light-colored regions for the furnace anneals). The temperatures of both furnace heat treatments were chosen to mimic the peak temperatures that were measured for diode

input powers at the onset of stress reduction (625 °C) and the maximum stress reduction (1000 °C). A four minute annealing time was chosen by using the rule-of-thumb, 1 hour/inch of thickness for austenizing steel. Since residual stresses can decrease with increasing time at a certain temperature according to the Larson-Miller equation [37], (see Discussion) a heat treatment duration of 30 minutes was chosen for the 625 °C anneal to increase the time at the maximum temperature by an order of magnitude compared to the in situ diode annealing.
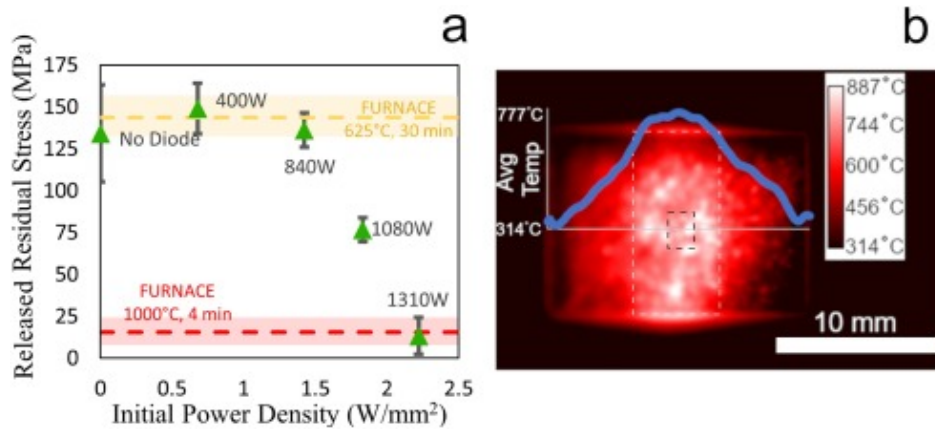
Figure 3.2: (A) Released stress as measured using BCM for each sample set. Each data point represents the average of three separate bridges built with identical conditions. Furnace annealed data is shown as dashed lines with the error bars shown as a colored band. (B) Average temperature of the diode annealing process along the length of the 1.83 W/mm^2 sample. The white dotted rectangle indicates the location of the overhang and the dotted black box represents the location of the temperature measurements in Fig. 3.3.

For the control bridges that were not subject to in situ annealing (No Diode), the average residual stress released by cutting through one leg was measured to be 134 ± 29 MPa. In situ annealing with an initial surface power density up to 0.98 W/mm^2 did not reduce the released residual stress. This power density corresponded to a surface temperature of roughly 625 °C (Fig. 3.3). This temperature is approximate because the measured temperatures of the bridge overhang sections varied by approximately 75 °C from layer to layer due to fluctuations in surface roughness and residual heat from the scanning laser. In comparison, the furnace anneal performed at 625 °C for 30 minutes also showed no measurable decrease in residual stress. Above 0.98 W/mm^2, the measured residual stress released due to cutting decreased with increasing diode energy input. At the maximum power density used in this work, 2.22 W/mm^2, the released residual stress was measured to be 13 ± 11 MPa, or approximately

10% of the measured residual stress in the control bridges. The peak temperature measured for this build was 1015 °C. Bridges furnace annealed at 1000 °C showed similar released residual stress (15 ± 7 MPa).
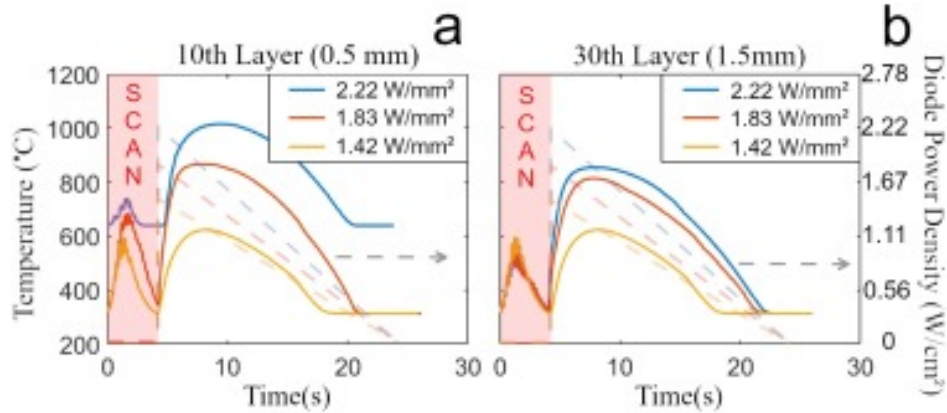
Figure 3.3: Temperatures at the center of the overhang (black dotted box in Fig. 3.2B) as a function of time for an overhang thickness of (A) 0.5 mm and (B) 1.5 mm. The initial peak is due to the passing of the scanning laser and the subsequent softer slope is due to the diode laser immediately afterwards. The dashed lines represent the power density of the diode projection as a function of time.

Although non-uniform temperatures can be expected even in a single block of material being heated by a uniform heat source, it was exacerbated in the bridges due to the varying thermal pathways that exist. The bridge supports have a better conductive pathway (vertically) to the build plate that acts as a heat sink and can therefore remain cooler than the overhang sections. The effect is seen in Fig. 3.2B. The temperatures shown in (Fig. 3.3 were measured at z = 0.5 mm and 1.5 mm (the 10th and 30th layers, respectively), where z = 0 mm is the bottom of the overhang. Temperatures were averaged over a 2×2 mm area in the center of the overhang section (black dotted box, Fig. 3.2B). The cooling rate was approximately 50 °C/s during the power ramp-down period for the highest power in situ annealing set (2.22 W/mm²). The lower power annealing experiments showed slightly lower cooling rates due to the fixed power ramp-down duration of 20 seconds.

Table 3.1 shows the process parameters used for the different bridge samples. The surface energy density of the scanning laser (Power/[Speed×Hatch]) was on the same order of magnitude as that of the diode anneal, but the power density was much lower (the focused

laser was approximately 5×10^5 J/mm^2). The listed annealing temperatures were estimated from the temperature measurements. Since the temperature of every layer could be not be measured due to data bandwidth limitations, and substantial variability existed in the layer-to-layer temperature, only a temperature estimate could be made.

The decrease in residual stress was overwhelmingly due to recovery and not recrystallization. EBSD crystal orientation maps of the No Diode, 2.22 W/mm^2, and 1000 ℃ furnace anneal bridges a shown in Fig 3.4A-C. No evidence of recrystallized grains or significant grain growth was observed; the grain size distributions from the three builds were comparable, with a mean equivalent grain diameter of approximately 9 μm (Fig 3.4D) for each sample set. Grain growth or recrystallization would shift the grain size distributions to higher or lower values, respectively. A slight change in the grain size distributions could be seen comparing the No Diode and 1000 ℃ furnace anneal bridges. Specifically, the number of small grains decreased slightly, a consequence of an increase in the number of grains with diameters near the mean value.

Optical and scanning electron microscope (SEM) images of the cross-sectioned bridges are shown in Fig 3.5. The melt pool fusion boundaries and cellular-dendritic solidification cells were clearly visible with sharp boundaries in the the No Diode sample. These solidification structures are typical of LPBF builds [38, 39]. In contrast, the fusion boundaries and cellular-dendritic solidification structure were diminished in the furnace annealed (1000 ℃) bridge due to chemical redistribution at elevated temperatures. In the 2.22 W/mm^2 diode annealed bridge, the solidification cells were visible at the top of the build but diminished toward the bottom. Since the lower layers were exposed to more diode annealing cycles than more recently-added higher layers, these lower layers experience more time at the temperatures required for solute diffusion, leading to solidification substructures with less distinct boundaries. This is similar to the observed decomposition of the martensitic phase in only the lower layers of LPBF AM Ti-6Al-4V alloys [40].

Vicker's microhardness measurements were also acquired along the bottom length of the
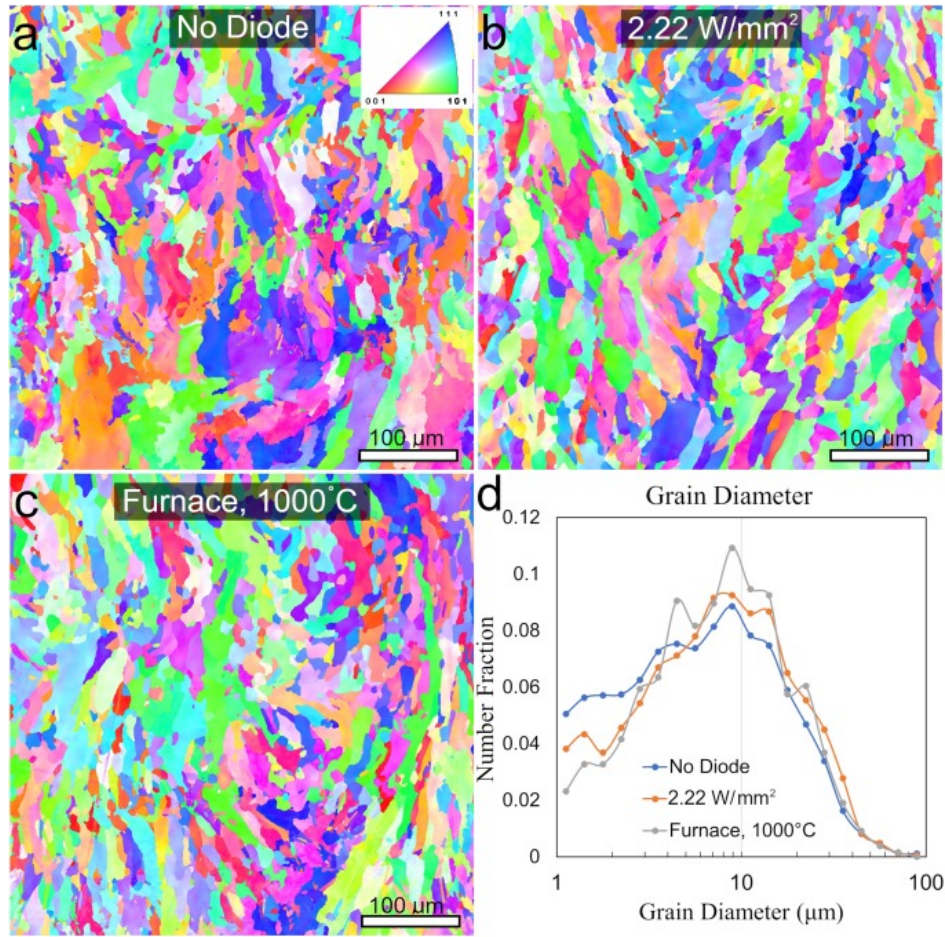
Figure 3.4:   Electron back-scatter diffraction crystal orientation maps of the (A) No Diode, (B) 2.22 W/mm² diode-annealed, and (C) 1000 °C furnace-annealed bridges. (D) The grain size distributions are comparable between the builds. The inset in A) shows the standard orientation triangle for an FCC material (316L stainless steel).

bridge overhang sections (dotted red line in Fig. 3.6A). The average hardness without diode annealing was 260 ± 13 HV. For the bridges annealed in the furnace at 1000 °C, the average hardness dropped to roughly 205 ± 7 HV. The hardness of the 2.22 W/mm² diode annealed bridge was measured along the top and bottom of the cross-section (dotted lines, Fig. 3.6A). As expected, the average hardness increased from 230 ± 13 HV at the bottom of the overhang to 243 ± 13 HV at the top.
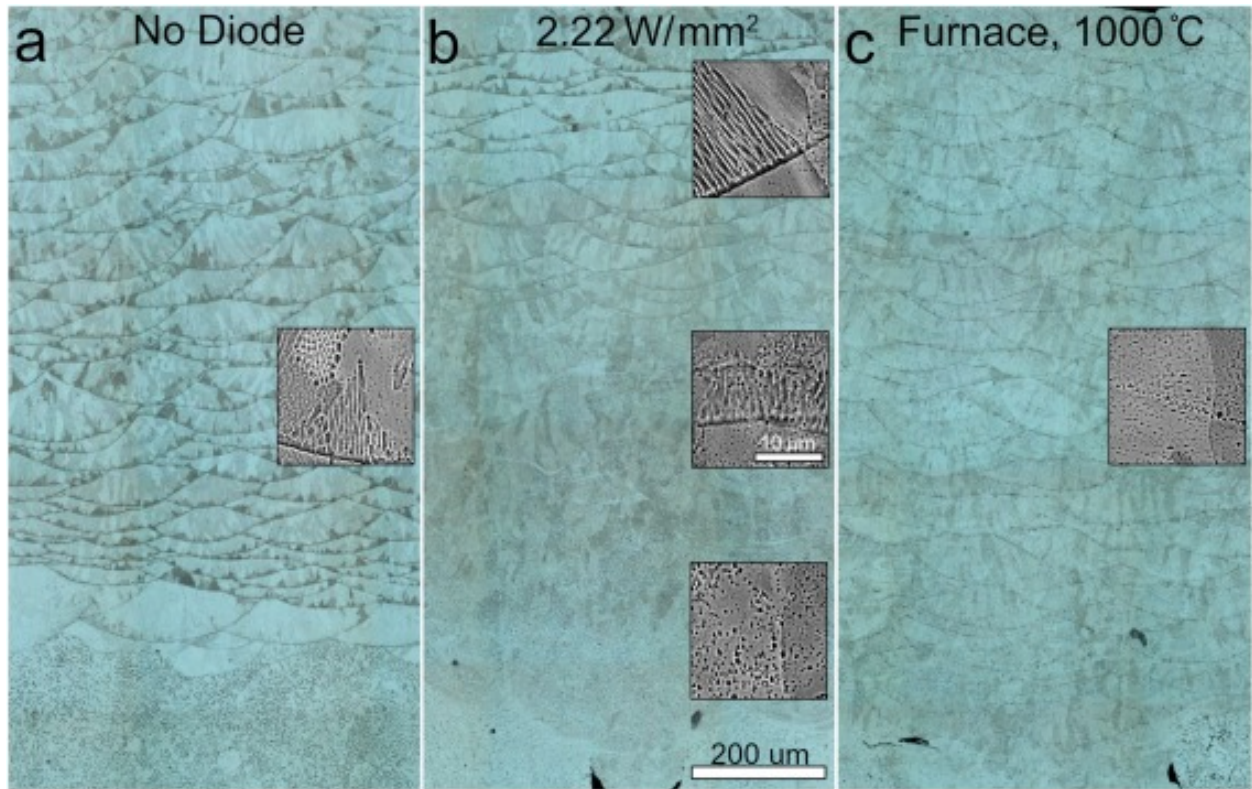
Figure 3.5: Optical and SEM images (inset) of etched bridge cross-sections. The vertical placements of the inset images correspond to their physical location within the bridge.

3.4 Discussion

3.4.1 Residual stress

The degree of residual stress relaxation is affected by the processing temperature, time held at that temperature, and the magnitude of the initial residual stress, which acts as a driving force for the process [41]. The experiments presented here attempted to remove the influence of the residual stress magnitude on stress relaxation by keeping the laser melting conditions identical from bridge to bridge. By doing this, the as-deposited state of the residual stress was consistent across the sample set. In addition to the residual stress, the microstructure and mechanical properties can also be affected by changes in the heat source or scanning strategy, which could affect the measurement of residual stress [12, 38, 42]. Due to the use of this consistent build strategy, changes in residual stress magnitude and

19

microstructure and are not considered. The focus will, instead, be on the effect of time and temperature on residual stress.

The residual stress in bridges built with in situ diode annealing was clearly reduced above a critical temperature, while no changes were noticed for insufficiently high diode power input. The critical temperature was found to be above 625 ℃. This finding correlates well with the yield stress of austenetic stainless steels, which decreases sharply above this temperature [37, 43]. The residual stress relief had a stronger correlation to the peak in situ annealing temperature reached than to the residence time at a particular temprature, as expected [41]. Dislocation annihilation and/or creep is the typical thermally-activated mechanism associated with the recovery process and can be described by the Larson Miller equation:

$$Th = T(20 + log(t)) \tag{3.1}$$

where Th is the relative thermal effect, T is temperature in Kelvin, and t is time in hours [37]. Based on this equation, temperature has a much greater influence on the relative thermal effect than time. For perspective, a 5% increase in temperature has the same effect as a tenfold increase in residence time.

The importance of the maximum temperature reached during in situ annealing was observed when comparing the furnace-annealed bridges (1000 ℃) to the 2.22 W/mm^2 in situ annealed bridges. The furnace-annealed bridges were heated from room temperature to 1000 ℃ at 33 ℃/min (ramp time of 30 min), held for 4 min, and ramped down to room temperature over 3 h. The peak temperature reached due to overshoot was approximately 1015 ℃. The peak temperature of the 22.2W/mm^2 diode anneal was also 1015 ℃ and the total time spent above 1000 ℃ was only several seconds per annealed layer (25 layers total). The estimated total time spent above 1000 ℃ was close to 90 s for the lowest layers, which decreases for the upper layers. Comparing the furnace anneal to the in situ anneal, a threefold increase in time above 1000 ℃ did not decrease the residual stress any further.

These results suggest that a significant reduction in residual stress can be achieved by

simply reaching the desired annealing temperature. While diode annealing was applied to every layer of the overhang (except for the first five layers) in this study, less frequent in situ annealing steps could be comparably effective. A conservative approach was taken here to ensure that the entire volume of material reached the desired temperature, but the frequency of the in situ anneal could be reduced to skip multiple layers, provided sufficient heating is applied to the surface for the underlying unannealed layers could still reach the desired temperature. Since each layer required an additional 20 s due to the in situ diode annealing, skipping multiple layers would significantly decrease the total build time. Additionally, the power ramp-down rate could be optimized. A faster cooling rate could still achieve lowered residual stress, but there could be a critical point at which increasing the cooling rate would introduce new thermal stresses and thus become the controlling factor in the final residual stress state.

3.4.2 Microstructure

Heating the AM bridges to temperatures above 1000 °C, whether by diode or furnace heating, did not result in significant grain growth or recrystallization. Since additively manufactured metals have been shown to resist recrystallization to higher temperatures than wrought metals, a lack of grain growth or recrstallization is not unexpected. This microstructural stability is attributed to the cellular solidification structure that is present in rapidly solidified metals [44]. The in situ annealing strategy leaves the cellular structure more intact than furnace annealing. This is evidenced by the SEM images of the bridges in Fig. 3.5. The cellular boundaries were less pronounced in the furnace-annealed bridge as compared to the $2.22 \, \text{W/mm}^2$ in situ diode-annealed bridge. If the residual stresses could still be relieved with fewer in situ annealing treatments, the solidification cellular microstructure could be better preserved.

Hardness is known to correlate with residual stress and increased dislocation density caused by plastic deformations in cubic metals [45, 46, 47, 48]. Hardness is also correlated to

a finer solidification structure and the chemical segregation that forms at dislocations in cell walls [39, 49]. The hardness distribution in the bridges followed the expectation of higher hardness with more chemical segregation/higher dislocation density: the furnace-annealed bridge retained the least solute segregation in the cell walls while the diode-annealed bridge retained slightly more solute segregation in the cell walls. In the diode-annealed bridge, solute segregation was better preserved in regions that experienced fewer annealing cycles (i.e., at the top of the bridge).

Despite the temperature variation over the bridge overhang section during in situ annealing (Fig. 3.2B), the hardness of the 2.22 W/mm^2 diode-annealed bridge did not vary greatly from the middle to the edge of the overhang (Fig. 3.6B). Its variation was similar to that of the No Diode bridge. This implies the temperature distribution does not need to be highly uniform to achieve reasonable residual stress reduction. Better uniformity of the temperature distribution could be achieved using the setup described by Matthews et al. [35], in which an optically addressable light valve was used to locally shape the intensity profile. Scaling the intensity over the print surface could achieve a more uniform temperature. This approach, or another means to fluidly control the annealing laser intensity, would also be useful for more complex geometries with disparate feature sizes and/or varied cross-sections throughout the build. Such intensity shaping will likely be necessary in an industrial setting because of the vast number of geometries amendable to manufacture by LPBF, but it will make direct production of nearly stress-free LPBF parts possible.

3.5   Conclusion

Residual stress control by in situ diode annealing during LPBF was successfully demonstrated for 316L stainless steel samples. By controlling the surface temperature of the material during the printing process, residual stress can effectively be reduced during LPBF, before the part is removed. A residual stress reduction of 90% was realized in stainless steel

316L bridge samples without grain growth or re-crystallization, and with only minor changes to the solidification structure. The peak temperature achieved during in situ annealing was found to have a much greater effect than the dwell time on the residual stress reduction. Further improvements can be made by optimizing the frequency of the in situ diode annealing process (i.e., number of layers per heating cycle), the ramp rates of the power profile, and the spatial distribution of the diode light intensity. This method could prove useful for decreasing risk during LPBF by directly manufacturing parts that a nearly stress-free, regardless of height, and removes the need for stress relieve post processing.
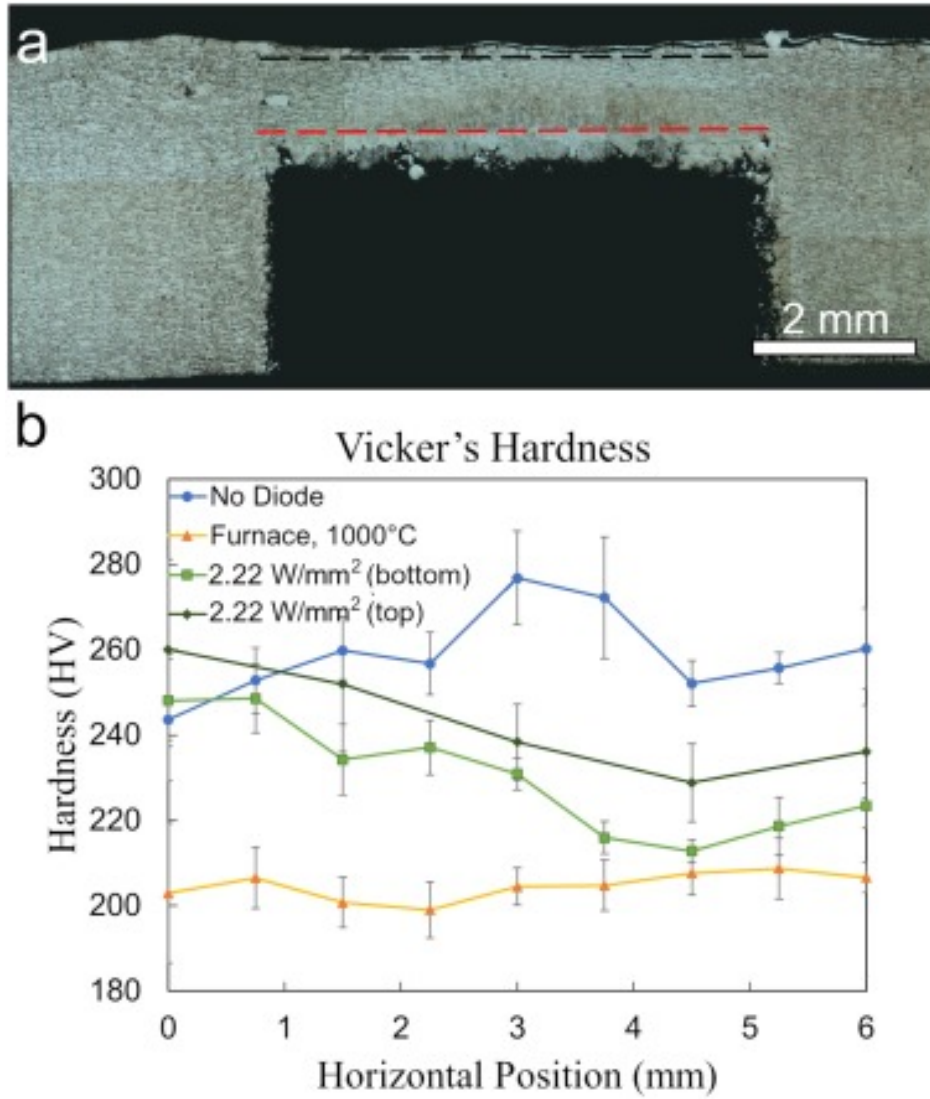
Figure 3.6: (A) Stitched optical image of a cross-sectioned diode-annealed bridge (2.22 W/mm^2) with locations of the hardness measurements marked. Measurements were taken along the red line for each sample. Hardness measurements were also taken along the black line for the 2.22 W/mm2 diode-annealed bridge. (B) The average Vicker's hardness along the bridge section in the different bridge builds.

4 Effect of in-situ Annealing on Residual Stress of 316L Stainless Steel - A Quantitative Study

4.1 Introduction

In this chapter, the effect of in-situ surface layer heating on the reduction of residual stress is assessed in rectangular 316L stainless steel samples printed through the LPBF process. A set of high power (kW) laser diodes was used as the in situ heating source which illuminated the recently scanned and solidified surface layer with homogeneous intensity immediately after the surface layer was complete. It is hypothesized that this surface layer heating/cooling strategy will introduce sufficient annealing into the LPBF process to achieve residual stress reduction, with the magnitude of stress reduction dependent on the degree of heating and the resulting thermal history. Residual stress is determined in samples subject to differing annealing strategies using two complementary stress measurement techniques, neutron diffraction and the contour method. Thermomechanical modeling is also performed to estimate the residual stress, providing a useful comparison with the experimental results. By utilizing these specific measurement and simulation techniques, the understanding of in situ surface layer annealing beyond that of the prior study using only BCM is advance. Additionally, an assessment of varied annealing strategies is made, comprised of annealing less frequently, to determine whether residual stress reduction could be accomplished more

economically.

A version of this chapter is published in *Additive Manufacturing* as:

4.2 Methods

4.2.1 Experimental setup

This study used rectangular block specimens built with dimensions of approximately 20 mm (L)×10 mm (W)×10 mm (H) on build plates 25.4 mm in diameter and 12.7 mm thick (Fig. 4.1D). Thicker build plates were selected than those used in the previous chapter (6.35 mm) to prevent potentially catastrophic warping due to an anticipated higher magnitude of residual stress. The scanning laser was held at a constant power and speed of 250 W and 278 mm/s, respectively. These parameters were chosen to maximize part density (above 99%) as well as minimize evaporation from the melt pool due to its proximity to the build window. Layers were scanned using a single contour pass around the perimeter and a crosshatch scan strategy within the interior where the scanning vectors were angled 45° with respect to the longitudinal axis of the part was rotated 90° between each layer.

For samples that were annealed in situ, the diodes illuminated the build area immediately after the focused melting laser finished its scan (Fig. 4.1C). The diode light was imaged from the mask plane onto the recently scanned and solidified material while the adjacent powder was not illuminated. Applying the diode illumination in this way ensures consisten densities and dimensions across samples. The diodes were initially applied at their maximum set power levels, followed by varying power ramps (Table 4.1). An example of a diode annealing power profile is provided in Fig. 4.2. The individual power profiles were chosen based on the

maximum achievable in-situ annealing temperature for a given diode laser power level.

Table 4.1: Processing parameters for the printed samples and their measured annealing temperatures. Stress measurements were made along the edge plane using neutron diffraction for samples listed in **bold**.

Diode Laser Power (W)	Maximum Diode Power Density (W/mm²)	Soak Time (s)	Ramp Time (s)	Diode Energy Density (J/mm²)	Approximate Annealing Temperature (°C)	Length (mm)	Width (mm)	Height (mm)
0	**0**	**0**	**0**	**0**	**N/A**	**20.12**	**10.30**	**11.23**
2600	4.42	0	5	11.05	700	22.46	10.20	11.31
2600	**4.42**	**2**	**5**	**19.90**	**1000**	**19.84**	**10.23**	**10.40**
3000	5.10	10	0	51.01	950 (every 5 layers)	19.86	10.15	12.08

4.2.2   Thermal measurements

Thermal imaging was used to measure the surface temperature of parts throughout the annealing process. A commercial pyrometer (Omega IR2C) was used to measure the surface temperature of samples throughout the annealing process and was positioned to be orthogonal to the 3 mm thick anti-reflective BK7 optical viewing window (Fig 4.1B), approximately 50 cm from the build surface. This pyrometer used wavelengths between 400 and 1600 nm to measure an average temperature over a circular area of approximately 10 mm in diameter at the center of the top layer. An optical notch filter was placed over the pyrometer probe to filter out the diode light. The pyrometer was capable of two-color pyrometry, but due to the required optical filter (to filter the diode light), anomalous temperatures resulted when using two-color mode. Therefore, the one-color mode was used after calibrating the emissivity.

Emissivity calibrations were performed by spot welding a thermocouple to the bottom of a 25.4 mm diameter 316L stainless steel disk of 500 μm thickness and insulating the bottom of the disk with 25.4 mm thick alumina wool. A thin disk was used to minimize the temperature drop between the top surface to the thermocouple on the underside. The diodes were then turned on to provide a heat source to the top side of the disk. The emissivity (0.45) was adjusted until the pyrometer and thermocouple readings were within 20 ± 2 °C throughout the entire measurement range (300-1300 °C). This calibration method was required because the diode light was within the measurement band of the pyrometer. Both
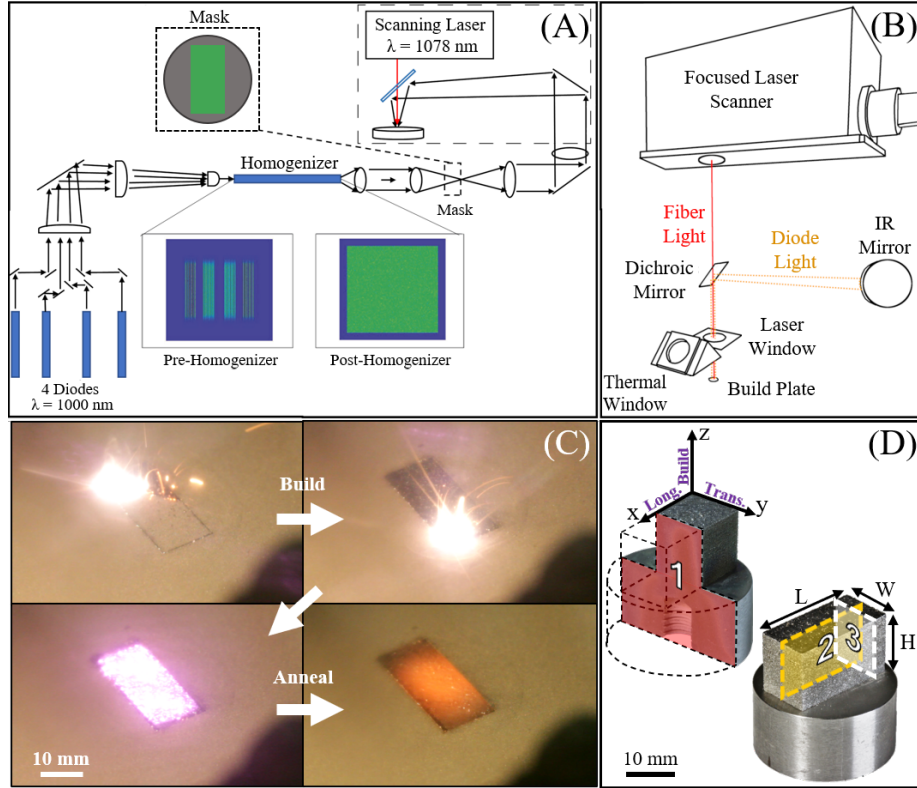
Figure 4.1: (A - B) Schematic of the diode annealing LPBF system. (C) Photos of the welding and annealing steps within the glovebox build chamber. (D) Photos of printed samples before and after sectioning, labeled with dimensions and stress directions (longitudinal, transverse, and build). Plane 1 represents the contour measurement plane while planes 2 and 3 represent the two neutron diffraction sampling planes within the uncut sample.

the presence of the optical filter and the operation of the diodes caused slight changes in the apparent temperature readings, which were minimized by using this calibration method. Calibration performed using a ceramic heater to heat the stainless steel disk and measuring the temperature on the top side with both the thermocouple and IR pyrometer did not yield accurate results when using the diodes to heat the surface.

4.2.3 Residual stress characterization

Two independent stress characterization approaches were carried out in the study presented in this chapter, specifically the contour method and neutron diffraction. In the contour method, the samples were sectioned using wire electrical discharge machining (EDM), relieving the internal stresses along this cut plane and creating two mirror-imaged surfaces.
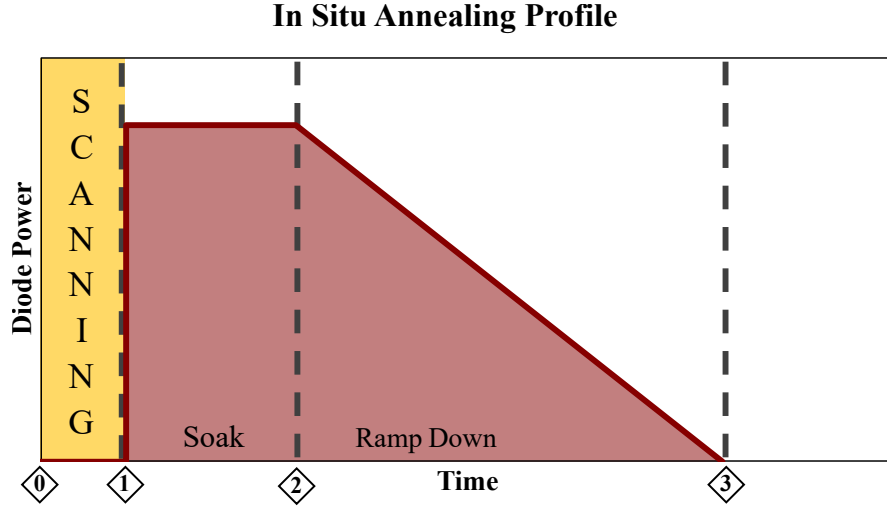
Figure 4.2: An example of a diode annealing power profile. (0) The fiber laser is scanning and welding the loose powder (1) Welding ends and laser diode emission initiates at full power and maintains for the duration of the soak (2) Soaking ends and the diodes ramp down from maximum power to 0 W (3) Annealing is complete.

Without being removed from their build plates, the as-printed samples were securely clampled and sectioned down the middle, orthogonal to the long axis of the samples at plane 1 (see Fig. 4.1D). All cutting was performed using a 152 µm (0.006 in.) diameter brass wire at 726 µm/min (0.03 in./min). A Keyence VR microscope profile scanner was used to optically measure height contour data on a grid of points with approximately 60 µm spacing in each direction. The surface contour data was processed in MATLAB and smoothed using a 3rd-order surface spline fit, which was then applied to a 3D representation in an elastic COMSOL Multiphysics® finite element model.

Neutron diffraction was also performed on these samples in order to measure the stresses beneath the surface of the samples. The neutron diffraction measurements were performed on the SMARTS instrument (Spectrometer for Materials Research at Temperature and Stress) at Los Alamos Neutron Science Center (LANSCE). A thorough description of the SMARTS instrument can be found in Bourke et al. [50]. The LANSCE accelerator produces a pulsed (20 Hz) incident neutron beam that results in a wavelength spectrum from 0.5 to 7.5 Å on the SMARTS instrument. During the measurements, the incident beam was masked by

boron nitride slits to a cross section of 2×2 mm^2. Two detector banks employing 3He tubes positioned at +90° and -90° from the incident beam were used to measure the diffracted neutrons using the time-of-flight (TOF) technique. The through thickness resolution was defined by a set of radial collimators with an acceptance length of 2 mm that were located in front of the detectors, and as a result, the presented diffraction measurements have a sampling volume of $2 \times 2 \times 2$ mm^3. To measure the three orthogonal strain components (ε_i), each sample was measured in two orientations with respect to the detectors, first horizontally and then vertically. The as-built averaged lattice strains were determined in the three orthogonal directions at points that were at least 1.75 mm away from the nearest surface to ensure that the sampling volume was always fully embedded within the sample. Applying Hooke's Law with a Young's modulus (E) of 200 GPa and a Poisson's ratio (ν) of 0.3 for 316L stainless steel, each of the three orthogonal stress components were calculated. For each sample, a total of 45 evenly-spaced measurements were made across the central longitudinal plane ($y = W/2$) of the as-printed sample in a 9×5 array, as indicated by Plane 2 in Fig 4.1D. Additionally, two samples (see Table 4.1) were measured along the transverse plane 1.75 mm from the edge of the part in a 5×5 data point array, as indicated by plane 3 in Fig. 4.1D.

4.2.4   Numerical simulations

The multi-physics finite element code, Diablo [51], developed at Lawrence Livermore National Laboratory, was used to perform thermomechanical simulations of the build process and forecast residual stresses for the given range of build and annealing conditions. Diablo is an implicit, Lagrangian code with distributed memory parallelism. The balance of energy is solved throughout the domain Ω:

$$\rho c_p \dot{T} = \nabla \cdot (k \nabla T) + r_{ext}, \text{ in } \Omega, \tag{4.1}$$

where ρ is the density, c_p is the constant pressure specific heat, T is temperature, k is the isotropic thermal conductivity, and ψ_{ext} represents the volumetric heat input from external sources such as the welding laser and the diodes. Boundary conditions are prescribed over the surfaces Γ_D, $\Gamma_{N_{top}}$, and $\Gamma_{N_{bot}}$ which represent the portion of the surface with prescribed Dirichlet and Neumann boundary conditions, respectively. They are expressed as follows:

$$
\begin{aligned}
T(\boldsymbol{x}, t) &= T_0, \text{on } \boldsymbol{x} \in \Gamma_D, \\
q(\boldsymbol{x}, t) &= \boldsymbol{q} \cdot \boldsymbol{n} = h_{bot}(T - T_\infty), \text{on } \boldsymbol{x} \in \Gamma_{N_{bot}}, \\
q(\boldsymbol{x}, t) &= \boldsymbol{q} \cdot \boldsymbol{n} = h_{top}(T - T_\infty) + \sigma_{SB}\varepsilon(T^4 - T_\infty^4), \text{on } \boldsymbol{x} \in \Gamma_{N_{top}}.
\end{aligned}
\tag{4.2}
$$

Here, Γ_D is the location where the build plate is bolted to the motion stage that controls movement in the build direction and $T_0 = 303$ K. $\Gamma_{N_{bot}}$ is defined as the remainder of the bottom surface of the build plate. As this portion is not directly attached to the substrate via the connecting bolt, a Neumann boundary condition with high convection coefficient of $h_{bot} = 1000$ W/(m^2 K) and $T_\infty = 303$ K was used to mimic heat transfer to the larger underlying substrate. On the top surface of the sample being built ($\Gamma_{N_{top}}$), convection and radiation to the external environment are modeled with emissivity, $\varepsilon = 0.3$ and $h_{top} = 40$ W/(m2*K). A depiction of the boundary conditions and mesh used for the part and build plate are shown in Figure 4.3A.

The mechanical system is governed by the balance of linear momentum given by,

$$
\rho\ddot{\boldsymbol{x}} = \nabla \cdot \boldsymbol{\sigma} + \boldsymbol{f}_b, \text{in } \Omega,
\tag{4.3}
$$

where ρ represents density, $\ddot{\boldsymbol{x}}$ is acceleration, $\boldsymbol{\sigma}$ is the Cauchy stress, and $\boldsymbol{f}_b$ represents body forces (neglecting gravity, $\boldsymbol{f}_b = 0$). A zero displacement Dirichlet boundary condition is

applied to where the build plate is affixed to the motion stage,

$$\boldsymbol{u}(\boldsymbol{x}, t) = 0, \text{on } \boldsymbol{x} \in \Gamma_D. \tag{4.4}$$

The stress is calculated via a strain rate independent plasticity model with linear isotropic hardening, as described in Hodge et al. [34]. Thermophysical and mechanical properties for 316L SS are also provided in Ref. [34].

In order to perform simulations at the physical layer size, h-type adaptive mesh refinement (AMR) is used [52]. The refinement is programmed to occur in a layer-wise manner, where all refinement/de-refinement occurs at the activation of each new layer. Three levels of isotropic pre-refinement were performed on the part, which is initially meshed with $0.4 \times 0.4 \times 0.4 \text{ mm}^3$ elements. As the element size is halved in each direction during each refinement step, the resulting element size is $0.05 \times 0.05 \times 0.05 \text{ mm}^3$. This allows for activation of 50 µm layers, as is true for the physical process. As each new layer is added, elements at a prescribed number of layers below the top surface are de-refined to minimize the total degrees of freedom in the problem, as illustrated in Fig. 4.3B. Further details regarding the AMR algorithm are provided in Ref. [53].

Despite using AMR to improve efficiency, simulating each individual laser melting pass remains too computationally expensive to be practical. Thus, the simulations are sped up by applying heat uniformly over an entire layer at once, a technique previously shown capable of producing relatively accurate residual stress predictions [54]. The amount of heat applied is calculated such that the total amount of energy deposited is equal to that supplied in the physical process. The volumetric power input during the laser melting portion is given as,

$$\psi_{ext,laser} = \frac{P_a}{Ad} = \frac{1}{t_{flash}} * \frac{\alpha_{melt} P_p}{hvd}. \tag{4.5}$$

In this equation, P_a refers to the layer agglomerated power, P_p refers to the physical process value, h is hatch spacing, v is scan speed, d is layer thickness, and A refers to the cross-

sectional area of the part (200 mm^2). The duration of power application (t_{flash}) is set to 0.1 seconds, which is long enough to allow for complete melting of the new layer. The effective absorptivity value during keyhole melting (α_{melt}) is equal to 0.7, which was determined via experimental measurements in Trapp et al. [55].

To model the diode heating phase, energy is again input over the entire top layer,

$$\psi_{ext,diode} = \frac{\alpha_{diode}P_{diode}(t)}{Ad}.$$

(4.6)

where $P_{diode}(t)$ is the applied diode power as a function of time. The absorptivity during diode heating (α_{diode}) is set to 0.3, which is close to the bare plate absorptivity value for 316L SS since the material has already solidified by this point. Similarly, other process parameters such as the inter-layer time were kept equal to that of the physical process.

(A)   (B)
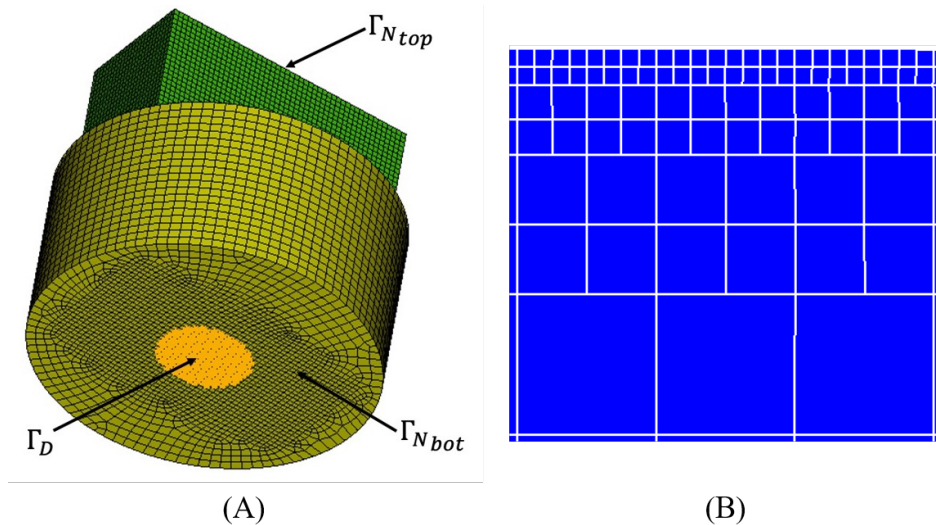
Figure 4.3: (A) Depiction of the boundary conditions and initial mesh for the build plate (yellow) and printed block (green). (B) Two-dimensional illustration of the mesh showing three levels of refinement, ranging from 50 to 400 µm in edge length.

4.3   Results

Contour measurements were performed for each sample listed in Table 4.1, where samples were sectioned along the central transverse axis using wire EDM (plane 1 in Fig. 4.1D), providing a map of the longitudinal stress in this central plane ($x = L/2$). Though an uncertainty analysis was not performed in this study, Olson, et al. [56] carried out a validation study of a previously developed contour method single-measurement uncertainty estimator [57] and found that modeling error was the largest contributor to the total uncertainty in their measurements while displacement measurement errors had a negligible contribution. This uncertainty was found to be related to elastic modulus, which for the case of 316L stainless steel is approximately 25 MPa ($125 \times 10^{-6}E$) for interior locations and 50 MPa ($250 \times 10^{-6}E$) for locations within 1 mm of the sample boundary. The contour plots in Fig. 4.4 display the longitudinal stresses normal to the cut surface of each printed sample, with the horizontal and vertical locations of the stresses normalized to the width and height of each sample (Table 4.1). Positive (red) and negative (blue) values represent tensile and compressive stresses, respectively. When looking at these longitudinal stresses over the entire cut printed surfaces, reduction in residual stress from in-situ annealing is apparent. There was a clear stress magnitude reduction with increased annealing temperature towards the bottom of the samples, at the interface between the printed sample and the build plate. As expected, the stresses were symmetric about the central vertical axis of the printed samples. Based on these contour measurements, comparable stress reduction was achieved when annealing less frequently (950 ℃ / 5 layers) as opposed to annealing every layer (1000 ℃). There was a reduction in overall compressive stress towards the bottom of the samples near the build plate, though the peak stresses closest to the corners remain relatively unchanged. However, there was not a significant reduction in stress near the edge of the annealed samples ($y = 0$ or W). Data near the side edges still showed compressive stresses ranging from -100 MPa near the top of the annealed samples to -600 MPa near the corners at the base of the samples.

When comparing results from the No Anneal and 700 °C samples in this plane, there was not a significant reduction in stress near the upper edge ($z = H$), while there wass such a reduction at the lower edge ($z = 0$).
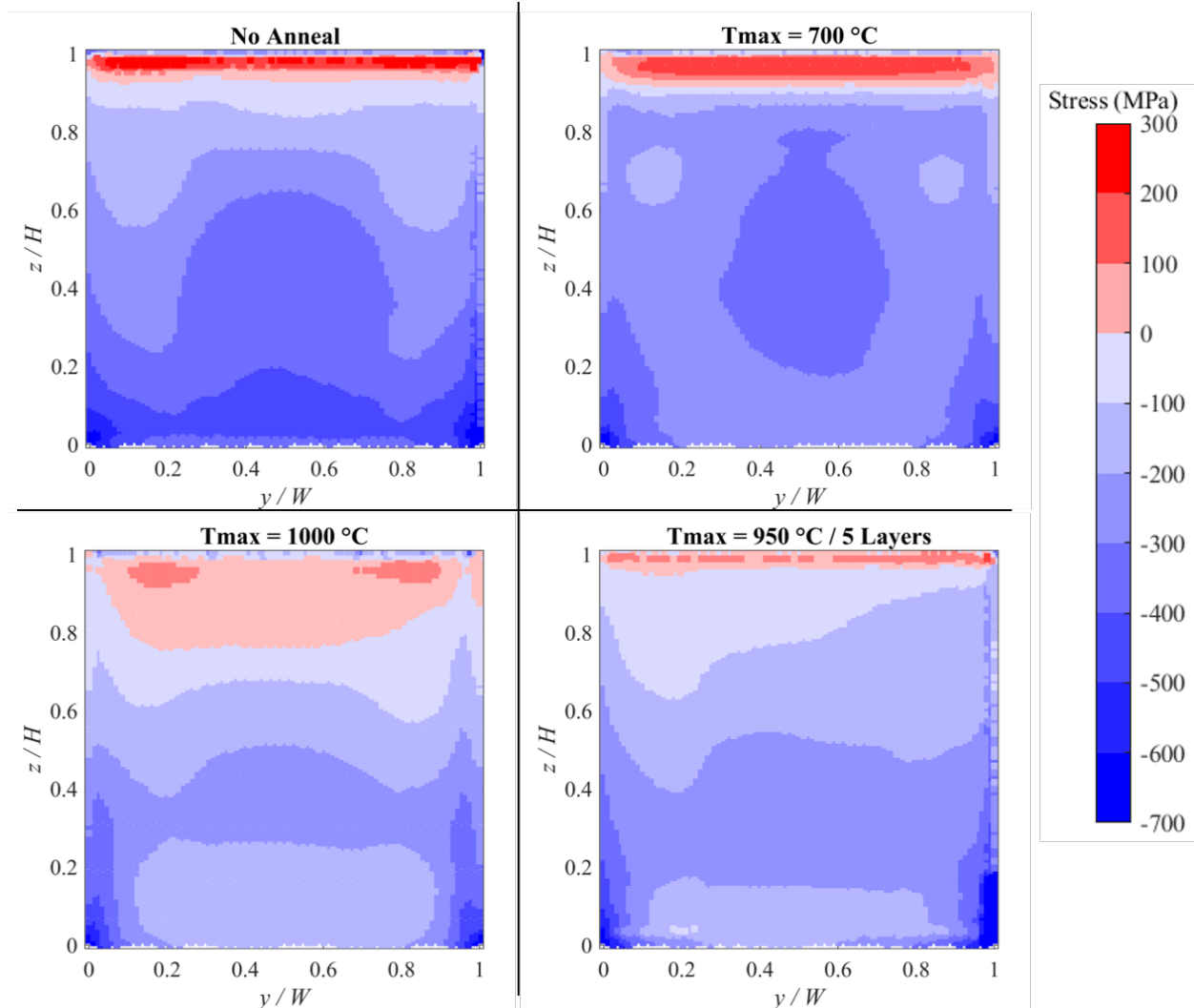
Figure 4.4: The longitudinal stress of printed parts as measured using the contour method. Measurements were taken along the cut surface at $x = L/2$ (Plane 1 in Fig. 4.1D).

Neutron diffraction measurements were made along the central longitudinal plane located at $y = W/2$ for each sample (Plane 2 in Fig. 4.1D). These neutron diffraction measurements were subject to some experimental uncertainty, which partially derives from the statistical standard deviation of the Rietveld refinement analyses. The resulting stress uncertainties, which propagate from the strain uncertainties, are approximately ± 14.6 MPa on average

with a maximum uncertainty of ± 35.9 MPa. Similar to the contour measurements shown in Fig. 4.4, the surface plots shown in Fig. 4.5 display an overall reduction in longitudinal stress throughout the neutron diffraction measurement plane with increased annealing temperature. There was a reduction in compressive stress in the longitudinal direction at the center of the printed samples as annealing temperature is increased. There was also a reduction in compressive stresses near the bottom of the samples, but data is not available close to the sample boundaries (closer than 1.75 mm from all edges) due to the constraints of neutron diffraction. Overall, there was a noticeable reduction in the magnitude of the residual stresses over the entire central longitudinal plane. Once again, the stress state of the sample annealed every 5 layers at 950 ℃ was very similar to the sample annealed every layer at 1000 ℃.
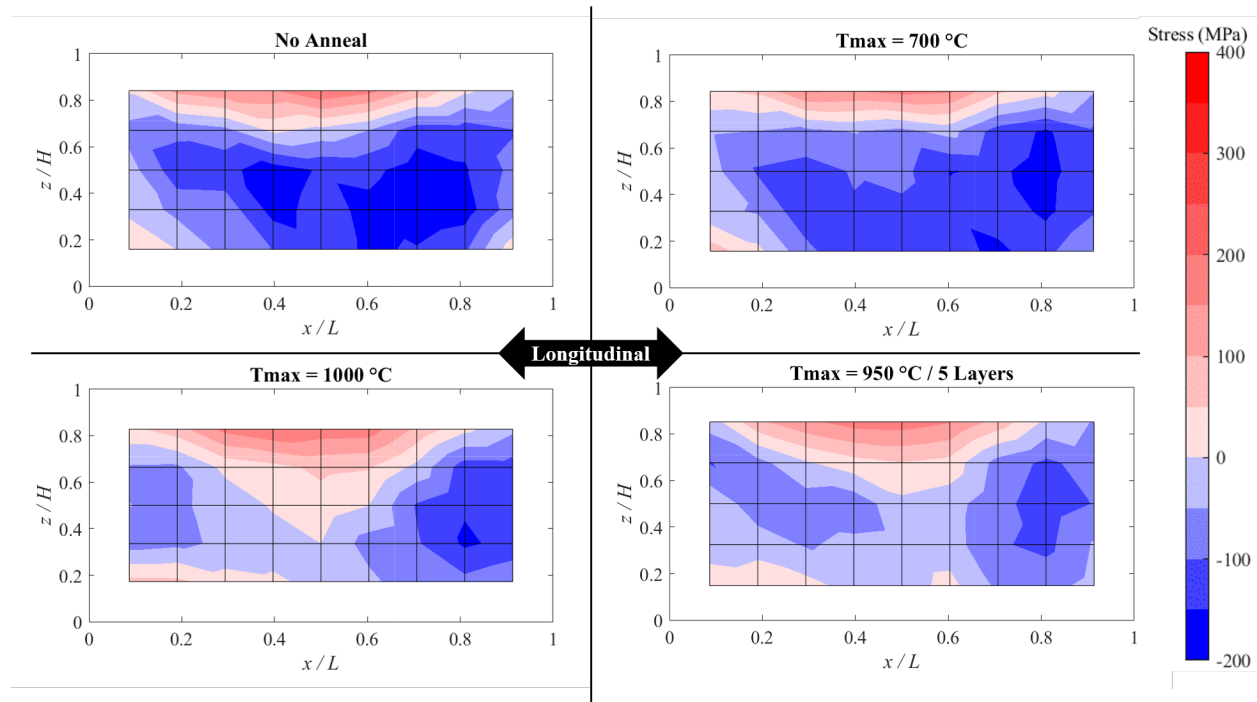
Figure 4.5: Longitudinal stress of samples measured using neutron diffraction at $y = W/2$ (Plane 2 in Fig. 4.1D).

Figure 4.6 compares the contour and neutron diffraction measurement data to simulation results. Stresses are compared along the central vertical axis of the printed block. This axis was chosen due to it being at the intersection of the central transverse and longitudinal planes

$(x = L/2, y = W/2)$, along which the contour and neutron diffraction data were sampled, respectively. There was generally good agreement between experimental data obtained using neutron diffraction, contour method, and model predictions. Data obtained from neutron diffraction and the contour method are closely matched while the modeling data deviated slightly for higher temperature samples, showing larger stress magnitudes at the top and bottom of the samples. When comparing the measurements near the top of the sample (1.75 mm from the top surface, or $z = 0.825H$) neutron diffraction data shows the stresses were invariant to annealing, with each sample displaying tensile stresses of approximately 200 MPa. The most noticeable reduction in stress occurred at the bottom of the sample, closer to the build plate. When comparing the samples built with the greatest difference in annealing conditions (No Anneal and 1000 ℃), the stress for the sample annealed to 1000 ℃ was -24 MPa for the contour measurement closest to the build plate ($z = 0$) while the sample built without any annealing had a -285 MPa compressive stress at this same location, which indicates a stress magnitude reduction of over 90%.

In addition to the measurements of the longitudinal stress, neutron diffraction was also used to measure residual stresses in the transverse and build directions. A comparison of the three orthogonal stress components is plotted in Fig. 4.7 with all data points taken along the central axis shown in Fig. 4.7D. There is an observable decrease in stress magnitude with increased annealing temperature, with the most significant reduction present in samples annealed above 700 ℃. This trend is predicted in the simulation results, which have a strong agreement with the results of the neutron diffraction measurements. The correlation between stress reduction and annealing temperature is particularly evident at the center of the samples ($x = L/2$) for the longitudinal and build stress components, with contour measurement results plotted for comparison in this same location (Fig. 4.7A). When comparing the sample built without in situ annealing (No Anneal) to the sample that was subject to the highest annealing temperature (1000 ℃), there is a stress change from compressive towards zero by 160 ± 21 MPa in the build direction and 183 ± 18 MPa in the longitudinal direction. The
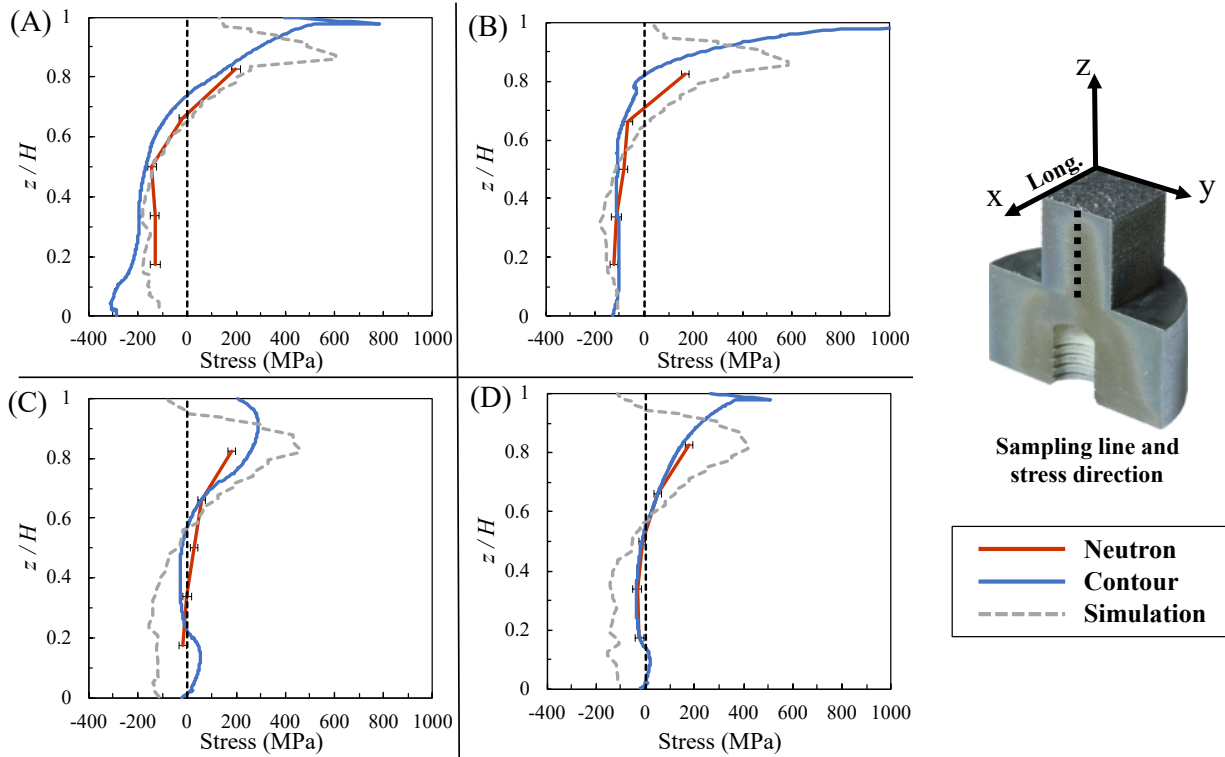
Figure 4.6: A comparison of longitudinal stress as determined by neutron diffraction, the contour method, and simulations. Data points are taken from a straight line in the z direction at the center of the samples $(x = L/2, y, = W/2)$. (A) No Anneal, (B) 700 °C, (C) 1000 °C, & (D) 950 °C / 5 Layers.

measured stress state of the sample annealed every 5 layers (950 °C/5 layers) is very similar to that of the sample annealed every layer (1000 °C) in all three directions. Even though the simulations predict a relatively small reduction in transverse stress with increased annealing temperature, this trend is less clear in the corresponding neutron diffraction results (Fig. 4.7B).

Neutron diffraction measurements were also performed near the short edge ($x = 1.75$ mm) of two of the specimens and the resulting build stresses are plotted in Fig. 4.8. As predicted by the simulation, stresses in the build direction were tensile at the bottom of the sample, with a region of compressive stresses near the top of each of the samples. For the sample annealed to 1000 °C, the compressive zone at the top of the sample grew in both size and in stress magnitude, while the tensile stresses in the bottom corners decreased in magnitude from 411 ± 15 MPa of tensile stress to 170 ± 13 MPa after annealing. This stress distribution

38

for the 1000 ℃ annealed sample differed from its simulated counterpart, which displayed an overall reduction in stress magnitudes, but the size of the respective stress zones remained relatively unchanged.

4.4 Discussion

The final residual stress state of printed parts can be influenced by several factors within the LPBF process including laser scan speed, laser power, and scan strategies, each of which drives the thermal gradients that cause stress. Additionally, complex or multi-component builds are also affected by the "jump" choices made when applying the scanning across the entire layer of a build. In this study, build surfaces were directly heated between build layers to both reduce stress in the prior layers and to provide a preheat that reduces the temperature gradient in subsequent layers. By keeping all other build parameters constant, densities remain consistent, the influence of solidification on the results is minimized, and the sole focus solely was on the influence of the annealing strategies.

There was a clear reduction in longitudinal and build stresses when annealing above a critical temperature, as seen in Fig. 4.7, which correlates to a previously observed decrease in yield stress of austenitic stainless steels above 650 ℃ [58]. The temperature dependence of the mechanical properties became visible when comparing the experimental and simulated results in Fig. 4.6, particularly when contrasting the lower temperature samples to those annealed to higher temperatures. The model appeared to overestimate the stresses above 700 ℃, which may be due increased uncertainty in material properties at higher temperatures [43, 58, 59]. There were no significant reductions in stress for the samples annealed below this temperature.

When reducing the frequency of layer annealing, there was still a similar stress reduction when compared to samples annealed every layer within that same temperature range. In the case of the print parameters for the sample shown in Fig. 4.6D, this means there was sufficient

stress reduction even though the total annealing time was roughly 71% shorter than that of a sample annealed every layer. Through the simulation for the sample heated to 950 °C every 5 layers, at a height of $z = 0.7H$), it was found that the maximum temperature at the surface was 985 °C and the temperature 500 µm below it was 936 °C. Given that the heat penetrated sufficiently for the temperature 10 layers below the surface to be within 50 °C of the maximum surface temperature, it seems that sufficient annealing can be accomplished when heating in intervals of at least 10 layers (500 µm), double that tested in this study.

The effect of the penetration depth of the surface annealing can also be seen when comparing stress reductions near the base of the samples versus the top. In Fig. 4.6, there was less residual stress reduction near the top surface of the sample ($z > 0.7H$) than the lower portion of the sample with increasing annealing temperature. The contour measurements at the very base of the samples ($y = 0$) decreased with each increase in annealing temperature, from -285.9 MPa for the No Anneal sample to -24.2 MPa for the 1000 °C sample, a reduction of over 90%. Meanwhile, those same samples experienced only a 47.6% reduction in stress near the top ($y = H$), decreasing from 396.2 MPa for the No Anneal Sample to 207.5 MPa for the 1000 °C sample. This can be attributed to the fact that the lower layers of the samples were subject to a higher number of annealing cycles than the layers closer to the top of the sample due to the penetration depth of the surface layer annealing. It is likely that the tensiles stress at the top of the in-situ annealed samples (Fig. 4.4) remained intact because the material in this upper region of the sample spent less time at maximum annealing temperature than the material below it. These observations are similar to the extent of martensite decomposition observed in LPBF of Ti-6Al-4V [60, 40], where repeated thermal cycles provided sufficient time and energy for the martensite in lower layers to decompose, whereas the martensite remained present in the top layers.

In the quest to achieve stress-free parts without the need for post-processing, a strategy to completely remove these stresses will need to be developed. To make up for the top layers spending less time at maximum annealing temperatures, a final prolonged soak (in addition

to the standard in situ annealing) could be performed to further relieve the stresses at the top of the part. A final prolonged soak to remove the stresses at the top of the part could be carried out to help reduce the stresses in this region of the part. To further reduce the stresses within the rest of the part, a reduced thermal gradient during the in-situ annealing process is needed. Because of the uniform illumination intensity on the top surface of the sample, some degree of lateral temperature gradients are present during annealing. Furthermore, temperature gradients into the thickness of the part are unavoidable due to the heat flux from the surface. Further strategies will need to be developed to tailor the annealing profile to achieve the lowest thermal gradients possible throughout the parts and reduce stresses to the lowest degree possible in as-built parts.

While the stress reduction trend apparent in experimental results correlates well with simulation results, there was not consistent agreement in stress magnitude and spatial distribution. An example of such a disagreement can be observed in the case of the neutron diffraction measurements made on the $x = 1.75$mm plane (Fig. 4.8), where there was a difference in build stress for the 1000 °C sample. The compressive zone in the top of the sample was both larger in size and in magnitude for the experimental results than the simulation results. This may be due in part to the nature of the diode projection onto the surface layer of the sample and the fact that it may not be totally uniform, particularly near the edges. There was a taper in intensity near the edges of the diode projection due to slight beam clipping from the mask and the overall sharpness of the projection. Also, the diode projection was made slightly smaller than the area of the top surface to ensure that none of the loose powder adjacent to the build area was subject to the surface annealing, as this could lead to unwanted melting or sintering of the powder and cause issues with spreading on subsequent layers. Since the numerical model simulated heat application to the entire surface, these non-ideal diode projection conditions could be the cause for the discrepancy between the experimental and simulated results close to this edge of the sample.

Though the samples were annealed with consistent laser power throughout the build,

surface layer monitoring revealed that the maximum annealing temperature for each layer was not always the same. In the case of the 700 °C sample shown in Fig. 4.9, the maximum temperature at a height of 1.65 mm was 656 °C while the temperature at 10 mm is 776 °C, a difference of 120 °C. This temperature difference can in large part be attributed to proximity of the surface layer to the build plate and a lack of thermal buildup after just 33 layers (1.65 mm). However, temperatures can vary between successive layers, as was the case for the peak temperatures at layer heights of 6.25 mm and 6.30 mm, which were 750 °C and 709 °C, respectively. This is a temperature difference of 41 °C between annealing steps that are just one layer (50 μm) apart. Given the penetration depth of the surface annealing, such temperature fluctuations will not impede residual stress reduction when annealed well above the critical temperature, but this could be an issue at lower temperatures. Upon close visual observation during printing, there seemed to be a correlation between surface roughness and annealing temperature. Since this annealing process relies on optical absorption of the diode laser energy, the roughness of the top surface plays a significant role. Smoother and more reflective surfaces will have lower absorption and will consequently reach lower annealing temperatures without increasing the diode laser power. Even when comparing subsequent heated layers, there can be temperature differences above 100 °C within one sample. This fluctuation in annealing temperature may explain some of the differences between the experimental and simulated residual stress results, particularly in the case of the higher temperature samples shown in Figure 4.6C,D. Since the mechanical properties of 316L stainless steel change dramatically above 700 °C, a fluctuation in annealing temperature of 100 °C can lead to significant discrepancies [59]. In an effort to find a correlation between roughness and annealing temperature, roughness measurements were made on the top surfaces of the printed samples using a microscope profile scanner (Keyence VR), but no clear correlation emerged. This was in part due to the surface roughness varying from layer to layer, so the roughness of the measurable final layer does not necessarily represent the roughness of all layers within the part.

In addition to the variation in surface roughness, the uniform heat input during the melting stage of the simulations could be a source of discrepancy between experimental and simulated results. This disagreement is particularly true near the top of the samples, as seen in Fig. 4.6, even for the non-annealed and lower temperature samples. In the simulations, heat was applied uniformly during the melting stage for each layer in order to cut down on simulation time, which is a technique that has been shown to produce reliable residual stress predictions in the past [17, 54]. However, the inaccuracies of this uniform heat distribution technique may be more visible in the upper layers where the material experiences fewer thermal cycles.

4.5   Conclusion

An analysis of the extent of stress reduction obtained using a novel and recently developed in-situ annealing process for LPBF was presented through spatial stress distribution maps of multiple planes within 316L stainless steel samples. These results were verified by employing multiple residual stress measurement techniques. These measurement techniques, in conjunction with the numerical simulation, showed that there is a stress reduction of over 90% near the base of the part when annealed every layer and there is an equivalent reduction in residual stress when parts are annealed every five layers, reducing the total annealing time by more than 17%. The results also revealed that in-situ annealing could be further explored to determine an optimal surface heating frequency to maintain stress reduction while minimizing processing time. Peak temperatures were hypothesized to be influenced by surface roughness, though the average annealing temperature for a given diode power level remained consistent. This method of stress reduction has the potential to significantly reduce distortions and improve print reliability of LPBF by building well-annealed parts irrespective of height and could eliminate the need for stress relief post processing.
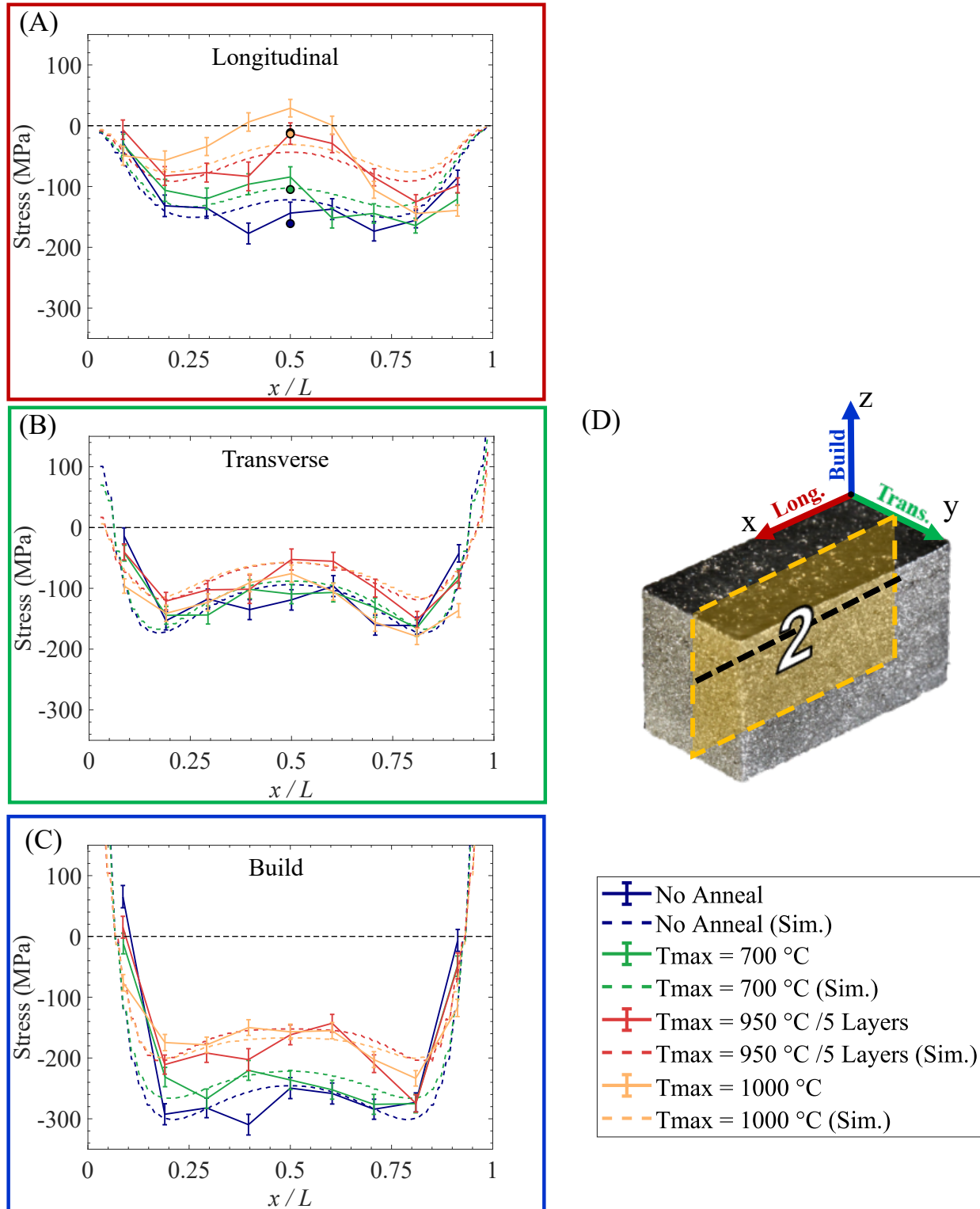
Figure 4.7: (A - C) Plots of the stresses measured through neutron diffraction as compared to simulations in each orthogonal stress direction. (A) Longitudinal stress at $x = L/2$ is compared to contour measurements in that same location, as indicated by the bold circles. (D) Each data point is sampled along the length of the printed sample at $z = H/2$ within the neutron sampling plane ($y = W/2$).
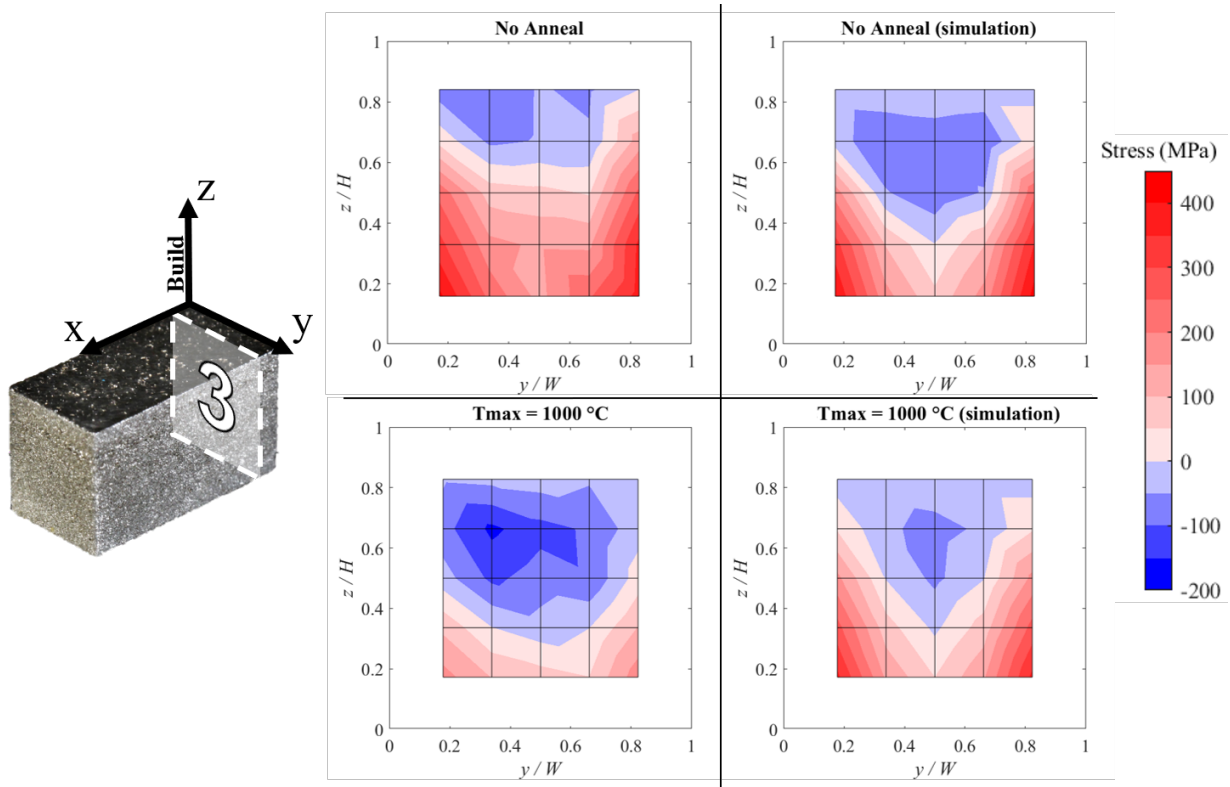
Figure 4.8: Build direction stresses data obtained through neutron diffraction experiments and the numerical model at $x = 1.75$ (Plane 3 in Fig. 4.1D).
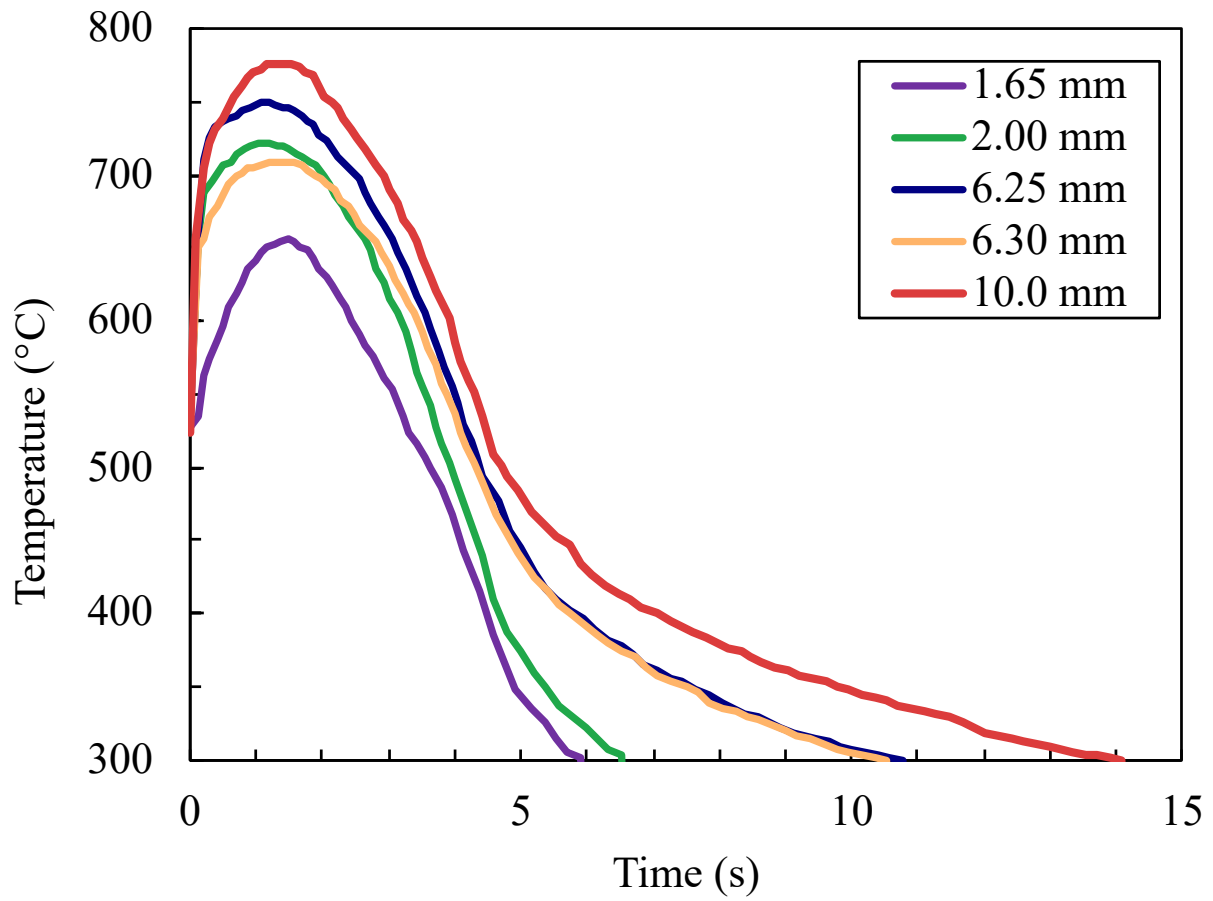
Figure 4.9: In situ annealing temperature at the center of the surface as a function of time at select heights.

5 Effect of Surface Layer Preheating and *in situ* Annealing on Residual Stress and Microstructure During LPBF

5.1 Introduction

Thus far, all of the presented samples have been subject to heating only after the scanning laser has finished welding (no preheating), adding an additional annealing step after each layer deposition. However, additional samples were produced in preliminary experiments and studied to observe the effect of surface layer preheating during LPBF on the microstructure of metal parts. Prior to the study presented in Chapter 3, a set of 316L stainless steel bridge samples was generated for bridge curvature method (BCM) measurements which contained samples that were heated before and *during* laser scanning (preheated). Bare plates of Ti-6Al-4V were also preheated using the diode lasers and were subsequently scanned by the fiber laser. The grain size, distribution, and microstructure were observed using a scanning electron microscope (SEM). Though the investigation into these samples was not as thorough as in previous chapters, the results found here indicate that the use of laser diodes for large surface area heating enables a degree of microstructure control by actively controlling the cooling rate and solidification rate within LPBF.

5.2 Methods

All samples covered in this chapter were generated using the custom LPBF machine equipped with an array of four diode lasers used for in situ surface layer heating. These samples were produced throughout various studies, using different laser scanning parameters. While the samples presented in Chapter 3 were exclusively 316L stainless steel bridges printed at 278 mm/s with a scanning laser power of 250 W, the bridge samples presented in this chapter were printed at 1000 mm/s. The bridges were printed with dimensions of 20 mm $(L) \times 11$ mm $(W) \times 5$ mm (H), having a 6 mm overhang, on build plates that were 25.4 mm (1 in.) in diameter and 6.35 mm (0.25 in.) thick. All bridge samples were printed in 50 µm layers and with hatches spaced 100 µm apart. The hatch directions were oriented 45°with respect to the long axis of the bridge and were rotated 90° between each layer.

Though all of the bridge samples shared identical scanning laser parameters, different diode annealing strategies were used and are listed in Table 5.1. The diode annealing strategies were chosen to explore the effect of laser preheating and ramp down on residual stress and microstructure, although over a relatively limited range of parameters. Nevertheless, the diode annealing strategies were generally chosen to make two determinations: (1) whether the microstructure of samples could be controlled by preheating the samples with the diode and (2) whether samples could experience residual stress reduction via in situ surface layer annealing. A plot of a diode annealing strategy in Fig. 5.1 highlights the basic steps taken in these diode annealing strategies. There is a brief ramping up period of 0.5 s in which the diode lasers transition from 0 W to maximum diode power (800 W). If a sample is to be subject to a pre-soak step to preheat the powder, then the diode lasers hold for 2 seconds before the scanning laser begins the layer melting. Once the scanning laser begins melting the powder, the diode laser continues to project at maximum power until the scanning is complete, at which point the diode lasers ramp down from maximum power to 0 W over 5 s or 10 s. Optical images of these steps are shown in Fig. 5.2.

In addition to 316L stainless steel bridges, plates of Ti-6Al-4V were also processed using in situ laser diode heating during welding by the fiber laser. The bare plates were 25.4 mm (1 in.) in diameter and 6.35 mm (0.25 in.) thick. A 20×11 mm^2 rectangular patch of melt tracks was scanned into the bare plates at 278 mm/s with a laser power of 250 W. One of the bare plate samples was heated with a diode power of 1500 W while the rectangular patch was melted by the scanning laser, which was immediately followed by a 10 s ramp down. Surface temperatures were recorded on these bare plate samples using a commercial pyrometer (Omega IR2C). The calibration procedure, setup, and usage of this pyrometer were identical to those outlined in Section 4.2.2.

After bridges were printed, the stress within the overhang portion of each bridge was evaluated using BCM. Surface profile measurements of the top of each bridge were captured before and after cutting using a Keyence VR optical microscope profile scanner. The difference in the corresponding height profiles before and after cutting was calculated, which was then treated as the deflection. The curvature of this deflection was used along with the overhang thickness to determine the relieved residual stress in the overhang using beam theory.

Once the residual stress measurements were complete, the 316L stainless steel bridges were completely removed from the build plate and sectioned along their lengths using a slow-speed diamond saw. The Ti-6Al-4V bare plate samples were also sectioned along the length of the rectangular patch. All samples were potted in epoxy and their newly-exposed surfaces were micropolished. The samples were imaged using a desktop SEM (Phenom Pro, Phenom World) and examined for differences across processing parameters.

5.3   Results

The measured bridge deflection after cutting and the resulting stress relief for each parameter set are shown in Fig. 5.3. Each data point represents an average of three separate

Table 5.1: Build parameters for the initial bridge sample set, which included preheated samples.

Ramp Up (s)	Preheat (s)	Ramp Down (s)	Total Diode Energy (J)
0	0	0	0
0.5	0	5	1130
0.5	0	10	1742
0.5	2	5	1620
0.5	2	10	2232
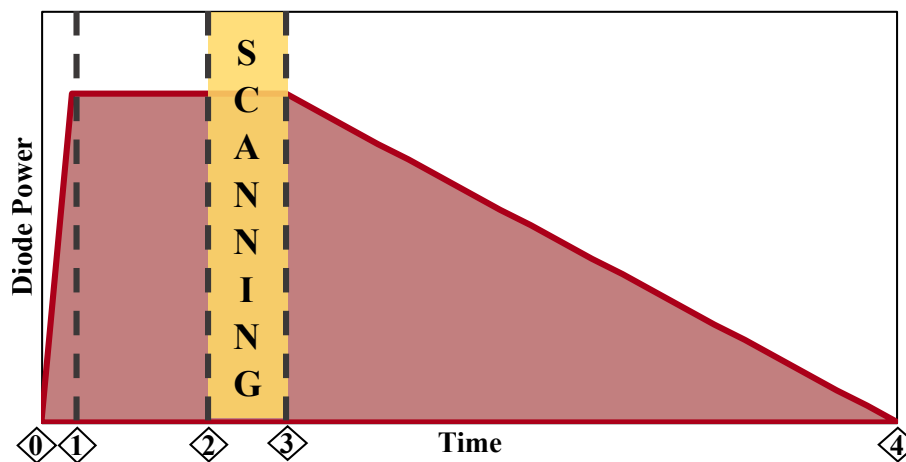
Figure 5.1: An example of a diode heating power profile. (0) The diode lasers initiate, ramping up to maximum power. (1) The diodes hold at maximum power before the welding begins, preheating the unfused powder. (2) The scanning laser welds the surface powder while the diode laser continues to heat the surface. (3) Welding is complete and the laser diode begins to ramp down to 0 W. (4) Laser processing is complete

bridge samples for each sample set, with the error bars in Fig. 5.3B corresponding to one standard deviation. The samples that were preheated with the diodes showed the smallest deflection across their overhangs (Fig. 5.3A), which reflects the smallest amount of residual stress and translates to a greater reduction in residual stress. There was an average residual stress release due to leg cutting of 272 ± 9 MPa for the samples produced without any diode heating. The sample set with the lowest displayed of residual stress release were samples subject to preheating and a 10 s ramp down at an average of 63 ± 16 MPa, which is a stress reduction of approximately 77%. As shown in Fig. 5.3B, the averaged preheated sample sets displayed lower levels of stress when compared to samples that were not preheated, despite one of the preheated sample sets exposing the bridges to less diode energy per layer. The
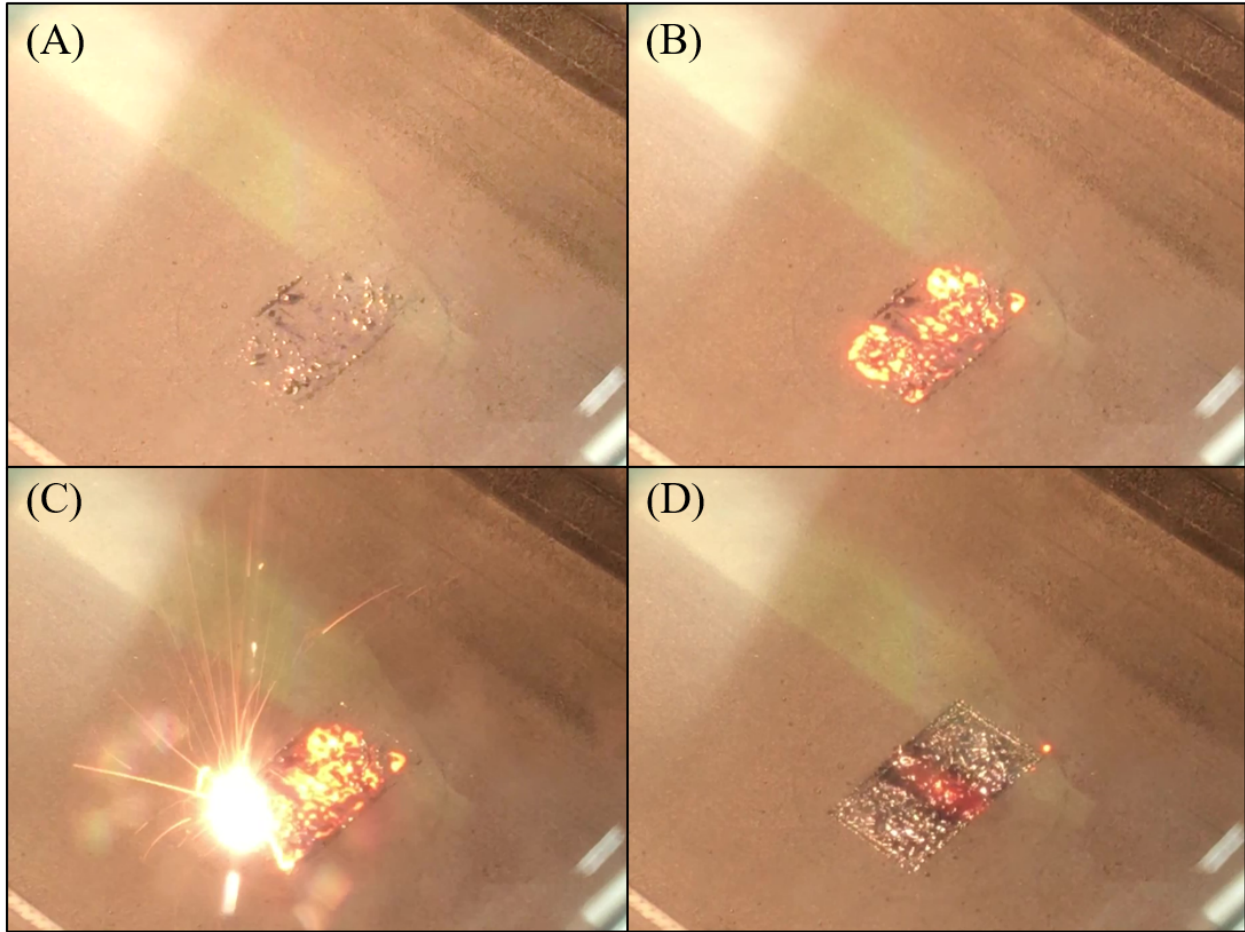
Figure 5.2: The printing process for preheated samples. (A) Freshly-spread powder. (B) Powder glowing due to being preheated by the diode lasers. (C) Scanning laser welds the powder while the diode laser continues to heat the surface. (D) The overhang in the center glows as the diodes ramp down from maximum power.

non-preheated bridges with a 10 s ramp down had an average stress of 109 $\pm$ 33 MPa while the preheated samples with a 5 s ramp down had an average stress of 71 $\pm$ 15 MPa even though they were exposed to 122 J less energy per layer.

SEM images of a portion of the overhang section - the area of interest - of the 316L stainless steel bridges are shown in Fig. 5.4 for select samples. The No Diode and non-preheated samples shown in Fig. 5.4A-B had nearly identical columnar grain structures. However, the overhang portion of the preheated sample shown in Fig. 5.4C showed clear signs of grain refinement, particularly towards the bottom of the overhang section with the presence of smaller equiaxed grains. SEM images of Ti-6Al-4V cross sections are shown in
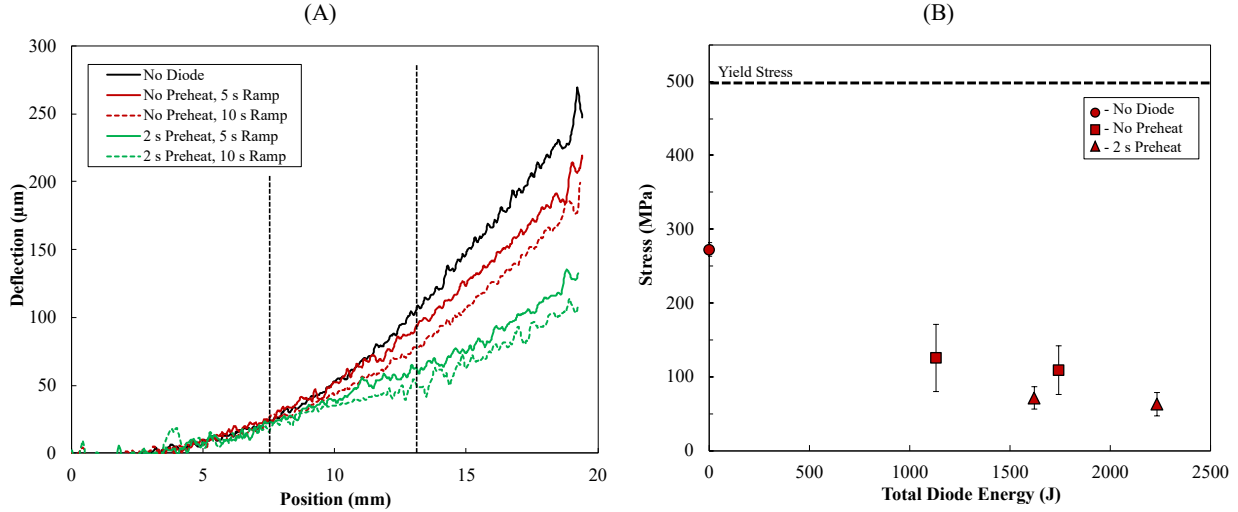
Figure 5.3: All data points and lines are an average of 3 repeat samples with identical parameters. (A) Deflection of the bridge samples as a function of position after one leg is removed from the build plate. The extent of overhang section is indicated by the vertical dashed lines. (B) Average bending stress for each sample set as calculated by the BCM as a function of the total energy projected in each layer by the diodes.

Fig. 5.5. The sample not exposed to any diode heating in Fig. 5.5A displayed the typical epitaxial grain phase distribution of α+α' in the weld tracks and the α+β phases present in the unaffected plate below. The microstructure of the preheated Ti-6Al-4V plate differed from the non-preheated plate, which is apparent when comparing their melt tracks. There were distinct α+β phases present in the preheated build plate, in both the melt track and the build plate beneath it. Additionally, heating the build plate has modified the ratio of α to β phases beneath the weld tracks, as seen when comparing this preheated plate to the non-preheated plate shown in Fig. 5.5.

5.4   Discussion

In Chapter 3, all of the grain sizes and structures of the 316L stainless steel bridge samples were comparable due to a lack of preheating (Fig. 3.4). This was to be expected since materials produced by LPBF are more resistant to recrystallization at elevated temperature than wrought material [44]. Here, a similar result was seen for samples that were not pre-heated (Fig. 5.4A-B) in that there were no signs of grain growth or recrystallization.
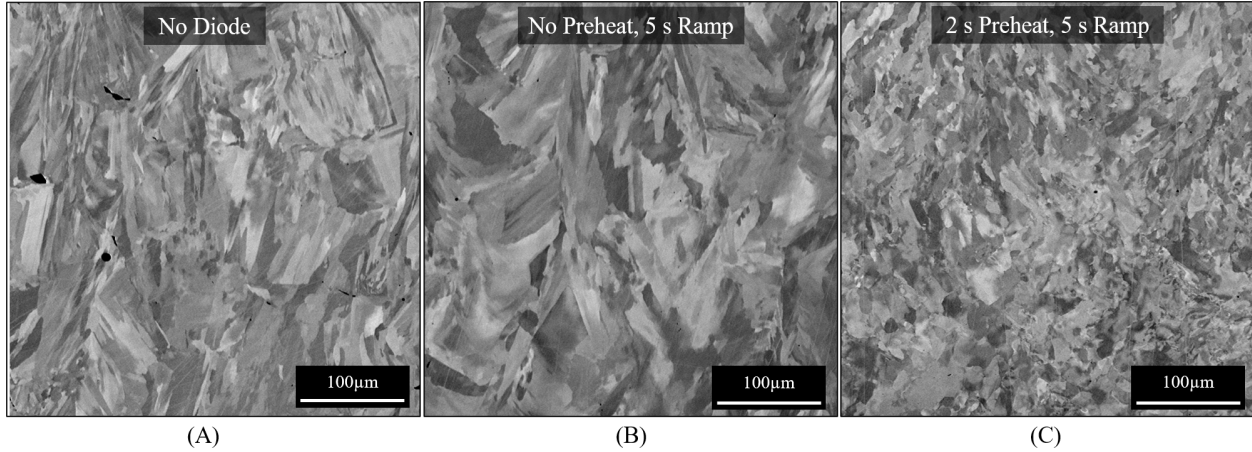
Figure 5.4: SEM images of overhang section of 316L stainless steel bridge samples with the following in-situ heating parameters: (A) No Diode (B) No preheat, 5 s ramp down. (C) 2 s preheat, 5 s ramp down.

There were clear signs of smaller more equiaxed grains for the preheated samples, which was likely a result of the lower thermal gradient experienced by these samples. The resulting microstructure during LPBF was largely affected by the ratio of thermal gradients (G) and solidification rate (R), or G/R [61]. As the temperature gradient decrease due to preheating the powder for 2 s, the resulting grain size decreased accordingly [61, 62].

The revelation of the residual stress reduction as a result of this in situ surface heating method on 316L stainless steel samples was very promising given that there was a reduction in stress of over 77% for the most disparate samples. However, upon sectioning select bridges for microstructure analysis, it was discovered that the samples had a higher porosity than expected. The remaining samples were removed from their build plates and the densities were measured using the Archimedes method and plotted in Fig. 5.6. Unfortunately, all of the bridge samples had relative densities (as compared to the density of the 316 stainless steel build plate) below the threshold of what is typically considered acceptable for LPBF (above 99%) due to using too high of a laser scanning speed, which is why their results were initially abandoned. While the ideal energy density for 316L stainless steel samples was later discovered to be 11.25 J/mm^2, the energy density for this set of bridge samples printed with a laser scanning speed of 1000 mm/s was only 3.125 J/mm^2 (over 72% lower). However, these density measurements, as shown in Fig. 5.6 indicate that there was a correlation between the
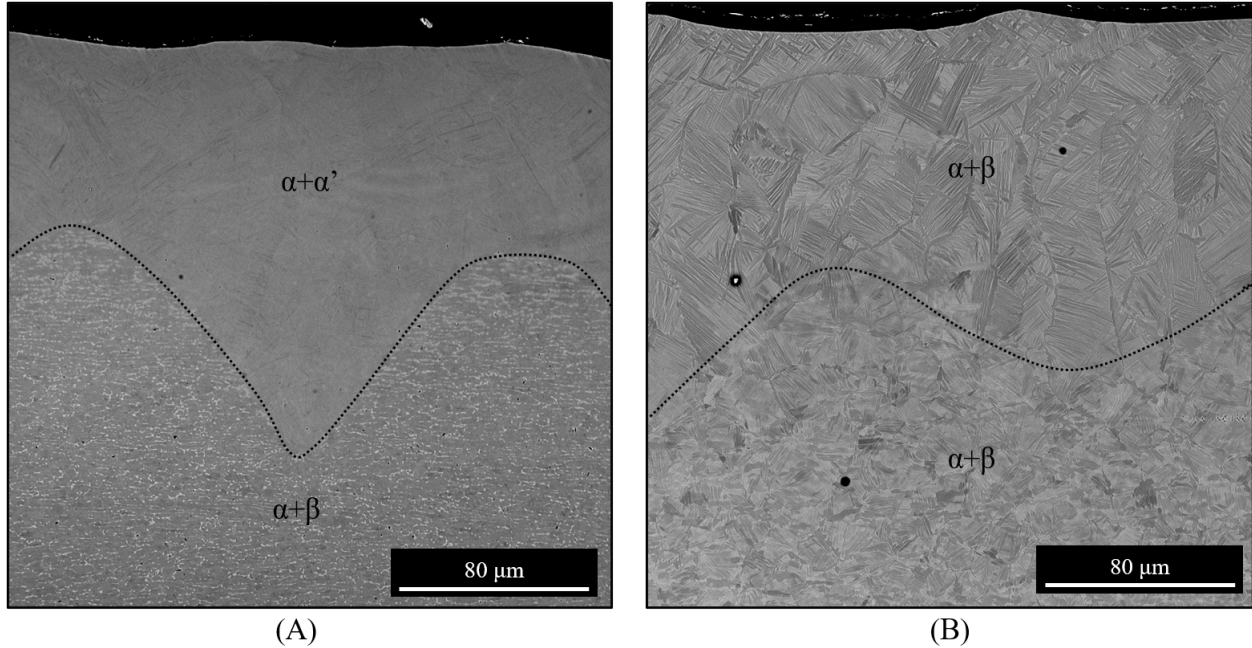
Figure 5.5: SEM images of sectioned and polished Ti-6Al-4V bare plates and their weld tracks with the fusion boundary highlighted by the dotted line. (A) No diode heating (B) Heated to 800 ˚C by the diodes during laser scanning.

amount of diode energy added to each layer and the relative density of the resulting part. The energy added by the diodes during the preheat heating and in situ heating for these bridge samples must have contributed to the increase in part density.

For the Ti-6Al-4V bare plates, the presence of α+β in the weld tracks indicates that the cooling rate was slow enough to bypass the α+α' structure that is typically present after LPBF of this material, as shown in Fig. 5.5. The thermal history of Ti-6Al-4V during LPBF has a major influence on the phases present after printing [1, 63], as seen in the continuous cooling transformation diagram shown in Fig. 5.7. The cooling rate of the heated bare plate in this study was approximately -16 ˚C/s, allowing the material to bypass the metastable α' martensite phase and leave behind just the α and β phases. This is a desirable composition for Ti-6Al-4V parts, because the strength of the α phase and the ductility of the β phase combine to produce a desirable material that is useful for many applications [64].
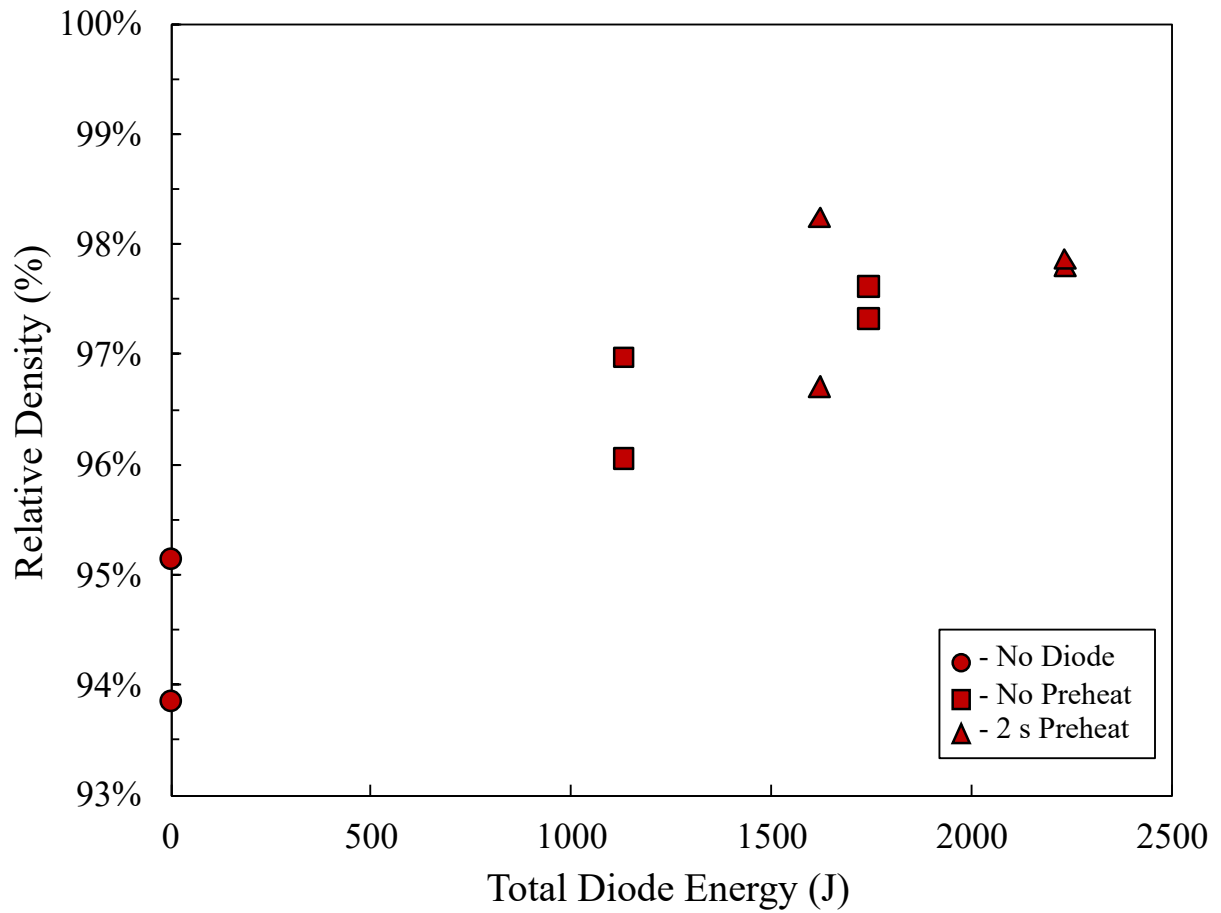
Figure 5.6: Relative density of 316L stainless steel bridge samples that were not sectioned and imaged using SEM.
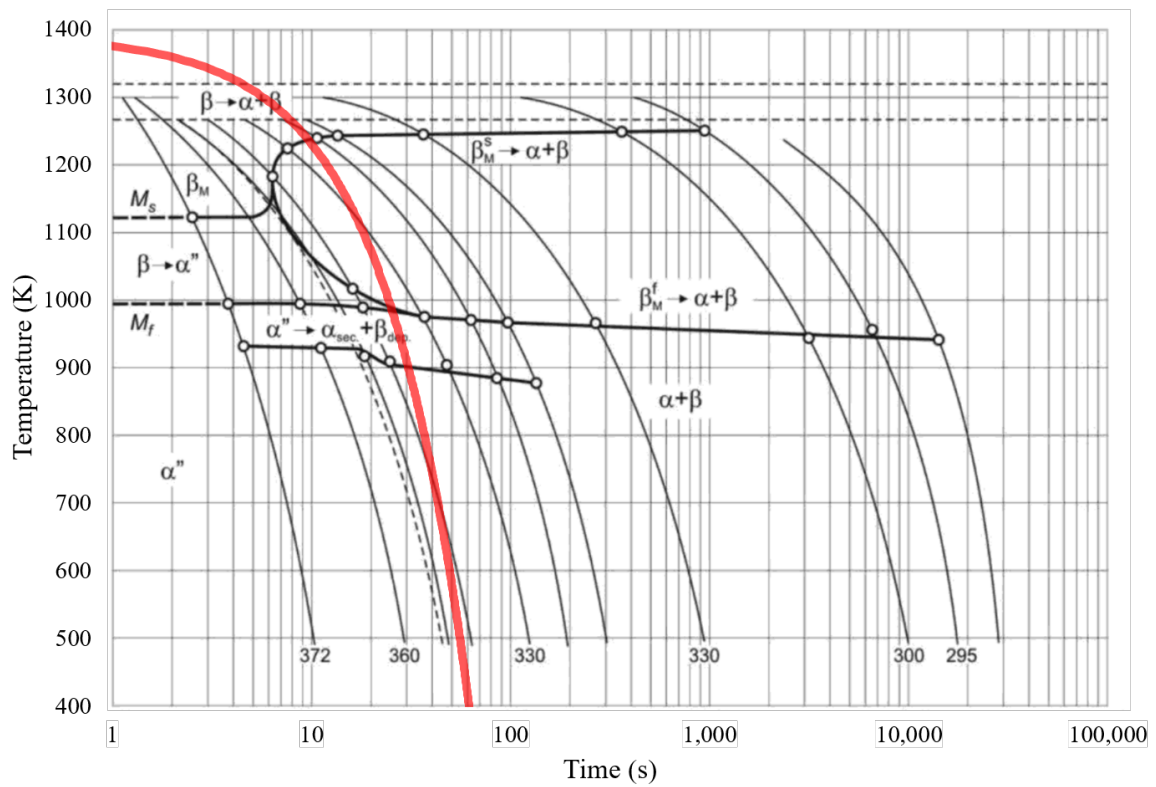
Figure 5.7: Continuous cooling transformation diagram for Ti-6Al-4V with the thermal history of the heated plate indicated in red (adapted from [1]).

5.5   Conclusion

The ability to affect the microstructure of LPBF parts was demonstrated by heating the surface layer prior to and during laser scanning. Bridge samples made of 316L stainless steel that were subject to preheating by a laser diode array showed grain refinement in the overhang section due to a decrease in the temperature gradient as compared to samples built without heating. Despite having less than ideal relative density, the surface layer heated 316L stainless steel samples experienced a decrease in residual stress, with the preheated samples having the lowest released residual stress. Less than ideal scanning parameters resulted in high porosity, but also revealed that the added energy from the in situ diode heating helped to increase the density of the bridge samples. This effect on part density could be studied further to produce more consistent parts, which would allow for further investigation into the microstructure control of 316 stainless steel during LPBF. Also, the surface of Ti-6Al-4V bare plates that were heated using diodes while being scanned with the fiber laser showed the presence of α and β phases in the weld tracks instead of the typical $\alpha + \alpha'$ microstructure because the cooling rate dictated by the diode heating was low enough to avoid typical martensite formation. The formation of α and β Ti-6Al-4V samples made through this in situ heating method in LPBF could be explored further with full builds. This demonstrated level of microstructure control could give rise to LPBF parts with tailored microstructures based on the diode masking procedure.

6   Conclusions

6.1   Summary of work

Laser powder bed fusion (LPBF) is a metal additive manufacturing process that utilizes a spot laser to melt metal powders to fabricate full parts, layer-by-layer. Localized rapid heating and cooling cycles are inherent to this repeated welding process, with the restriction of thermal expansions and contractions resulting in the build up of localized plastic strain and internal residual stresses. These residual stresses can cause macroscopic deformations in parts, warping, cracking, or even delamination from the build plate. With metal additive manufacturing having an ever-growing presence in the industrial space for generating geometrically complex parts, research into avoiding such catastrophic failures is of great interest. Methods such as build plate heating and build chamber heating have been implemented with LPBF to reduce the temperature gradients. Annealing in a furnace after building is often carried out to remove and remaining stresses. However, these techniques do not prevent the macroscopic deformations that may arise while printing large parts with geometries that extend far from the build plate.

This work investigated the effects of applying a novel in situ annealing method to LPBF. This annealing method differed from previous heating methods in that it heated the top surface of the sample instead of the build plate. This was achieved by using an array of laser diodes to apply an even-intensity projection onto the entire surface of 316L stainless steel parts. An initial study was carried out to verify the ability to achieve residual stress reduction using this in situ annealing method. Bridge samples were printed with identical

scanning parameters, treated with varying in situ annealing profiles, and compared to traditionally furnace-annealed bridges. Bridge curvature measurements showed that samples treated with the highest in situ annealing temperature achieved (approximately 1000 ℃) a stress reduction of 90% relative to the residual stress in samples not heated by the laser diodes. The results from the maximally in situ annealed bridge samples matched well with bridge samples heated to a similar peak temperature using the traditional furnace annealing method. Upon analyzing the results, it was found that the peak temperature achieved during in situ annealing had a greater influence on the degree of residual stress reduction than the dwell time. These bridge samples did not experience grain growth or re-crystallization, and there were only minor changes to the solidification structure.

While this initial study confirmed the ability to control residual stress by using laser diodes for in situ annealing, it only provided a rather qualitative assessment of the residual stress state of the samples after treatment. The study that followed analyzed the extent of residual stress reduction by investigating the spatial distribution of stress within 316L stainless steel rectangular samples printed using LPBF. After examining the internal stresses on multiple planes using neutron diffraction and the contour method, a stress reduction of over 90% was further confirmed. This level of reduction was achieved when annealing every layer as well as when annealing every five layers, confirming the ability to reduce the build time by skipping layers when annealing. All of these results were validated through numerical simulations. The results from each of these studies indicates that this method of stress reduction has the potential to significantly reduce distortions and improve the as-printed quality of parts produced using LPBF. Since the annealing is performed at the build surface, it is especially applicable to tall parts. This technique may also eliminate the need for stress relief post processing.

A brief investigation into utilizing in situ surface layer heating in LPBF to control microstructure was carried out for 316L stainless steel bridges and Ti-6Al-4V bare plates. The heated Ti-6Al-4V bare plate sample had a cooling rate low enough to bypass the typical

α+α' formation and processed weld tracks that consisted of lamellar α+β phases. The 316L stainless steel bridges that were preheated before scanning displayed grain refinement in their microstructure as compared to non-preheated samples due to a reduction in the temperature gradient during solidification. These samples were initially abandoned due to having too high porosity, but futher analysis of these samples revealed that preheating the surface layer actually increased the overall relative density of the bridge due to the added energy of the diode laser projection.

6.2 Future Work

There is still a lot of room for growth and development in the effort to anneal LPBF parts using the surface area heating technique presented here. The major findings in this study were largely limited to heating the surface of parts after welding, but it is possible to heat the surface of the powder before printing to reduce the temperature gradient during welding. This was attempted initially, but it was difficult to get consistent or predictable densities in samples that were treated in this way. It would be beneficial to obtain near full density (above 99%) preheated parts, since preheating is shown to allow for microstructure control.

This study mainly focused on 316L stainless steel builds, but there are several other alloy materials that have been printed using LPBF and it would be interesting to learn how they respond to this in situ annealing technique. Tests were performed on Ti-6Al-4V bare plates with in situ annealing, but full builds were not possible due to safety concerns of large reactive powder (Ti-6Al-4V) prints with the current method. In addition to printing with materials common to LPBF, this in situ annealing technique could enable the printing of materials that were previously not feasible to print. Materials that are prone to cracking during LPBF, such as tungsten, could possibly benefit from this in situ annealing method. By reducing the cooling rate, and thus the rate of contraction, cracking could be minimized

or potentially fully prevented.

Fixed masks were used to shape the light from the diode lasers in each of these studies, which limits the user to only annealing a fixed area. A major advantage that LPBF has over traditional manufacturing methods is the ability to fabricate complex geometries, so having the ability to anneal modular surface areas would be ideal. Annealing selective surface areas can be achieved with the use of optically addressable light valves (OALV), which have the ability to shape light that passes through them in real time [35, 65]. Behaving similarly to a projector, an OALV could anneal complex geometries and select areas, potentially enhancing mechanical performance.

Due to the fact that the system utilized in these studies was originally designed for research purposes, the build area is small (25.4 mm build diameter) relative to full scale commercial systems ($\approx$400 mm build diameters). If this approach is to be used in a full-scale industrial setting, the system will need to be capable of annealing a larger surface area. The logical step to scaling up this system would be to integrate more diode lasers into the surface heating. Using lenses to increase the projected area would decrease the intensity at the surface while keeping the total energy the same, so more diodes would be required to maintain an appropriate intensity. Instead of simply adding more diodes to the system, activated mirrors could be used alongside an OALV to direct uniform diode projections over the surface of the layers. This approach would enable annealing of larger and more complex geometries in LPBF.

Funding and Support

Bibliography

[1] Jan Sieniawski and Waldemar Ziaja. *Titanium Alloys: Advances in Properties Control.* BoD – Books on Demand, May 2013.

[2] William E. Frazier. Metal Additive Manufacturing: A Review. *Journal of Materials Engineering and Performance*, 23(6):1917–1928, June 2014.

[3] W. E. King, A. T. Anderson, R. M. Ferencz, N. E. Hodge, C. Kamath, S. A. Khairallah, and A. M. Rubenchik. Laser powder bed fusion additive manufacturing of metals; physics, computational, and materials challenges. *Applied Physics Reviews*, 2(4):041304, December 2015.

[4] Aiden A. Martin, Nicholas P. Calta, Saad A. Khairallah, Jenny Wang, Phillip J. Depond, Anthony Y. Fong, Vivek Thampy, Gabe M. Guss, Andrew M. Kiss, Kevin H. Stone, Christopher J. Tassone, Johanna Nelson Weker, Michael F. Toney, Tony van Buuren, and Manyalibo J. Matthews. Dynamics of pore formation during laser powder bed fusion additive manufacturing. *Nature Communications*, 10(1):1987, April 2019.

[5] Paul A. Hooper. Melt pool temperature and cooling rates in laser powder bed fusion. *Additive Manufacturing*, 22:548–559, August 2018.

[6] Özgür Poyraz and Melih Cemal Kuşhan. Residual Stress-induced Distortions in Laser Powder Bed Additive Manufacturing of Nickel-based Superalloys. *Strojniški vestnik - Journal of Mechanical Engineering*, 65(6):343–350, June 2019.

[7] Amanda S. Wu, Donald W. Brown, Mukul Kumar, Gilbert F. Gallegos, and Wayne E. King. An Experimental Investigation into Additive Manufacturing-Induced Residual Stresses in 316L Stainless Steel. *Metallurgical and Materials Transactions A*, 45(13):6260–6270, December 2014.

[8] J.P. Kruth, B. Vandenbroucke, J. Van Vaerenbergh, and P. Mercelis. Benchmarking of Different SLS/SLM Processes as Rapid Manufacturing Technicques. April 2005.

[9] J. P. Kruth, L. Froyen, J. Van Vaerenbergh, P. Mercelis, M. Rombouts, and B. Lauwers. Selective laser melting of iron-based powder. *Journal of Materials Processing Technology*, 149(1):616–622, June 2004.

[10] Yang Liu, Yongqiang Yang, and Di Wang. A study on the residual stress during selective laser melting (SLM) of metallic powder. *The International Journal of Advanced Manufacturing Technology*, 87(1):647–656, October 2016.

[11] Jean-Pierre Kruth, Jan Deckers, Evren Yasa, and Ruben Wauthlé. Assessing and comparing influencing factors of residual stresses in selective laser melting using a novel analysis method:. *Proceedings of the Institution of Mechanical Engineers, Part B: Journal of Engineering Manufacture*, March 2012.

[12] Peter Mercelis and Jean-Pierre Kruth. Residual stresses in selective laser sintering and selective laser melting. In *Rapid Prototyping Journal*, volume 12, pages 254–265. Emerald Group Publishing Limited, October 2006.

[13] John D. Roehling, William L. Smith, Tien T. Roehling, Bey Vrancken, Gabriel M. Guss, Joseph T. McKeown, Michael R. Hill, and Manyalibo J. Matthews. Reducing residual stress by selective large-area diode surface heating during laser powder bed fusion additive manufacturing. *Additive Manufacturing*, 28:228–235, August 2019.

[14] Pruk Aggarangsi and Jack Beuth. Localized Preheating Approaches for Reducing Residual Stress in Additive Manufacturing. *Proc. SFF Symp., Austin:*, January 2006.

[15] Loucas Papadakis, Dimitrios Chantzis, and Konstantinos Salonitis. On the energy efficiency of pre-heating methods in SLM/SLS processes. *The International Journal of Advanced Manufacturing Technology*, 95(1):1325–1338, March 2018.

[16] L. A. Parry, I. A. Ashcroft, and R. D. Wildman. Geometrical effects on residual stress in selective laser melting. *Additive Manufacturing*, 25:166 – 175, 2019.

[17] Michael F. Zaeh and Gregor Branner. Investigations on residual stresses and deformations in selective laser melting. *Production Engineering*, 4(1):35–45, February 2010.

[18] Liang Ma and Hongzan Bin. Temperature and stress analysis and simulation in fractal scanning-based laser sintering. *The International Journal of Advanced Manufacturing Technology*, 34(9):898–903, October 2007.

[19] Alexander Ulbricht, Simon J. Altenburg, Maximilian Sprengel, Konstantin Sommer, Gunther Mohr, Tobias Fritsch, Tatiana Mishurova, Itziar Serrano-Munoz, Alexander Evans, Michael Hofmann, and Giovanni Bruno. Separation of the Formation Mechanisms of Residual Stresses in LPBF 316L. *Metals*, 10(9):1234, September 2020.

[20] M. Strantza, B. Vrancken, M. B. Prime, C. E. Truman, M. Rombouts, D. W. Brown, P. Guillaume, and D. Van Hemelrijck. Directional and oscillating residual stress on the mesoscale in additively manufactured Ti-6Al-4V. *Acta Materialia*, 168:299–308, April 2019.

[21] Michael R. Hill. The Slitting Method. In *Practical Residual Stress Measurement Methods*, pages 89–108. John Wiley & Sons, Ltd, 2013.

[22] Michael B. Prime. Residual Stress Measurement by Successive Extension of a Slot: The Crack Compliance Method. *Applied Mechanics Reviews*, 52(2):75–96, February 1999.

[23] P. Pagliaro, M. B. Prime, H. Swenson, and B. Zuccarello. Measuring Multiple Residual-Stress Components using the Contour Method and Multiple Cuts. *Experimental Mechanics*, 50(2):187–194, February 2010.

[24] Bey Vrancken, Victoria Cain, Rob Knutsen, and Jan Van Humbeeck. Residual stress via the contour method in compact tension specimens produced via selective laser melting. *Scripta Materialia*, 87:29–32, September 2014.

[25] Mehdi Salem, Sabine Le Roux, Anis Hor, and Gilles Dour. A new insight on the analysis of residual stresses related distortions in selective laser melting of Ti-6Al-4V using the improved bridge curvature method. *Additive Manufacturing*, 36:101586, December 2020.

[26] Bjørn Clausen, Christopher R. D'Elia, Michael B. Prime, Michael R. Hill, Joseph E. Bishop, Kyle L. Johnson, Bradley H. Jared, Kyle M. Allen, Dorian K. Balch, R. Allen Roach, and Donald W. Brown. Complementary Measurements of Residual Stresses Before and After Base Plate Removal in an Intricate Additively-Manufactured Stainless-Steel Valve Housing. *Additive Manufacturing*, 36:101555, December 2020.

[27] D. W. Brown, A. Losko, J. S. Carpenter, B. Clausen, J. C. Cooley, V. Livescu, P. Kenesei, J.-S. Park, T. J. Stockman, and M. Strantza. In-Situ High-Energy X-ray Diffraction During a Linear Deposition of 308 Stainless Steel via Wire Arc Additive Manufacture. *Metallurgical and Materials Transactions A*, 51(3):1379–1394, March 2020.

[28] M. Strantza, R. K. Ganeriwala, B. Clausen, T. Q. Phan, L. E. Levine, D. Pagan, W. E. King, N. E. Hodge, and D. W. Brown. Coupled experimental and computational study of residual stresses in additively manufactured Ti-6Al-4V components. *Materials Letters*, 231:221–224, November 2018.

[29] Michael B. Prime and Adrian T. DeWald. The Contour Method. In *Practical Residual Stress Measurement Methods*, pages 109–138. John Wiley & Sons, Ltd, 2013.

[30] Adrian T. DeWald and Michael R. Hill. Residual stress in a thick steel weld determined using the contour method. Technical report, University of California Davis, November 2001.

[31] A. D. Krawitz and R. A. Winholtz. Use of position-dependent stress-free standards for diffraction stress measurements. *Materials Science and Engineering: A*, 185(1):123–130, September 1994.

[32] Mark R. Daymond. The determination of a continuum mechanics equivalent elastic strain from the analysis of multiple diffraction peaks. *Journal of Applied Physics*, 96(8):4263–4272, October 2004. Publisher: American Institute of Physics.

[33] Cheng Wu. Properties of Stainless Steel AISI Type 316L, 2020.

[34] N. E. Hodge, R. M. Ferencz, and J. M. Solberg. Implementation of a thermomechanical model for the simulation of selective laser melting. *Computational Mechanics*, 54(1):33–51, 2014.

[35] Manyalibo J. Matthews, Gabe Guss, Derrek R. Drachenberg, James A. Demuth, John E. Heebner, Eric B. Duoss, Joshua D. Kuntz, and Christopher M. Spadaccini. Diode-based additive manufacturing of metals using an optically-addressable light valve. *Optics Express*, 25(10):11788–11800, May 2017.

[36] Raya Mertens, Stijn Clijsters, Karolien Kempen, and Jean-Pierre Kruth. Optimization of Scan Strategies in Selective Laser Melting of Aluminum Parts With Downfacing Areas. *Journal of Manufacturing Science and Engineering*, 136(061012), October 2014.

[37] D.A. Cononico. Stress-Relief Heat Treating of Steel. 4A, August 2013.

[38] Tien T. Roehling, Sheldon S. Q. Wu, Saad A. Khairallah, John D. Roehling, S. Stefan Soezeri, Michael F. Crumb, and Manyalibo J. Matthews. Modulating laser intensity profile ellipticity for microstructural control during metal additive manufacturing. *Acta Materialia*, 128:197–206, April 2017.

[39] Y. Morris Wang, Thomas Voisin, Joseph T. McKeown, Jianchao Ye, Nicholas P. Calta, Zan Li, Zhi Zeng, Yin Zhang, Wen Chen, Tien Tran Roehling, Ryan T. Ott, Melissa K. Santala, Philip J. Depond, Manyalibo J. Matthews, Alex V. Hamza, and Ting Zhu. Additively manufactured hierarchical stainless steels with high strength and ductility. *Nature Materials*, 17(1):63–71, January 2018.

[40] W. Xu, M. Brandt, S. Sun, J. Elambasseril, Q. Liu, K. Latham, K. Xia, and M. Qian. Additive manufacturing of strong and ductile Ti–6Al–4V by selective laser melting via in situ martensite decomposition. *Acta Materialia*, 85:74–84, February 2015.

[41] George E. Totten, Maurice A. H. Howes, and Tatsuo Inoue, editors. *Handbook of residual stress and deformation of steel*. ASM International, Materials Park, Ohio, 2002.

[42] R. R. Dehoff, M. M. Kirka, W. J. Sames, H. Bilheux, A. S. Tremsin, L. E. Lowe, and S. S. Babu. Site specific control of crystallographic grain orientation through electron beam additive manufacturing. *Materials Science and Technology*, 31(8):931–938, June 2015.

[43] North American Stainless. *Long Prodcuts Stainless Steel Grade Sheet*. 2010.

[44] Thale R. Smith, Joshua D. Sugar, Julie M. Schoenung, and Chris San Marchi. Anomalous Annealing Response of Directed Energy Deposited Type 304L Austenitic Stainless Steel. *JOM*, 70(3):358–363, March 2018.

[45] S.C. Schroeder, J. Frankel, and A. Abbate. The Relationship Between Residual Stress and Hardness and the Onset of Plastic Deformation. Technical Report ARCCB-TR-95029, U.S. Army ARDEC, May 1991.

[46] M. Odnobokova, A. Kipelova, A. Belyakov, and R. Kaibyshev. Microstructure evolution in a 316L stainless steel subjected to multidirectional forging and unidirectional bar rolling. *IOP Conference Series: Materials Science and Engineering*, 63:012060, August 2014.

[47] Katsuji Tosha. Influence of Residual Stresses on the Hardness Number. pages 48–54.

[48] Ali A. H. Ameri, Nancy N. Elewa, Mahmud Ashraf, and Juan P. Escobedo-Diaz. General methodology to estimate the dislocation density from microhardness measurements. *Materials Characterization*, 131:324–330, September 2017.

[49] Q. Jia and D. Gu. Selective laser melting additive manufacturing of Inconel 718 super-alloy parts: Densification, microstructure and properties. 2014.

[50] M.A.M. Bourke, D.C. Dunand, and E. Ustundag. SMARTS – a spectrometer for strain measurement in engineering materials. *Applied Physics A*, 74(1):s1707–s1709, December 2002.

[51] J.M. Solberg, N.E. Hodge, M.A. Puso, S.T. Castonguay, R.K. Ganeriwala, and R.M. Ferencz. Diablo: A Parallel, Implicit Multi-physics Finite Element Code for Engineering Analysis User Manual. LLNL-SM-757180, Lawrence Livermore National Laboratory, 2018.

[52] L. Demkowicz, Ph. Devloo, and J. T. Oden. On an h-type mesh-refinement strategy based on minimization of interpolation errors. *Computer Methods in Applied Mechanics and Engineering*, 53(1):67–89, October 1985.

[53] Rishi K. Ganeriwala, Neil E. Hodge, and Jerome M. Solberg. Towards improved speed and accuracy of laser powder bed fusion simulations via multiscale spatial representations. *Computational Materials Science*, 187:110112, 2021.

[54] R.K. Ganeriwala, M. Strantza, W.E. King, B. Clausen, T.Q. Phan, L.E. Levine, D.W. Brown, and N.E. Hodge. Evaluation of a thermomechanical model for prediction of residual stress during laser powder bed fusion of Ti-6Al-4V. *Additive Manufacturing*, 27:489–502, 2019.

[55] Johannes Trapp, Alexander M. Rubenchik, Gabe Guss, and Manyalibo J. Matthews. In situ absorptivity measurements of metallic powders during laser powder-bed fusion additive manufacturing. *Applied Materials Today*, 9:341–349, 2017.

[56] M. D. Olson, A. T. DeWald, and M. R. Hill. Validation of a Contour Method Single-Measurement Uncertainty Estimator. *Experimental Mechanics*, 58(5):767–781, June 2018.

[57] M. D. Olson, A. T. DeWald, M. B. Prime, and M. R. Hill. Estimation of Uncertainty for Contour Method Residual Stress Measurements. *Experimental Mechanics*, 55(3):577–585, March 2015.

[58] Stress-Relief Heat Treating of Steel[1]. In Jon L. Dossett and George E. Totten, editors, *Steel Heat Treating Fundamentals and Processes*, pages 275–279. ASM International, 2013.

[59] American Iron and Steel Institute (last). *High-Temperature Characteristics of Stainless Steels*. Nickel Development Institute, April 2020.

[60] A. Zafari, M. R. Barati, and K. Xia. Controlling martensitic decomposition during selective laser melting to achieve best ductility in high strength Ti-6Al-4V. *Materials Science and Engineering: A*, 744:445–455, January 2019.

[61] John N. DuPont. Fundamentals of Weld Solidification. 6A:97–117, October 2011.

[62] Fuyao Yan, Wei Xiong, and Eric J. Faierson. Grain Structure Control of Additively Manufactured Metallic Materials. *Materials*, 10(11):1260, November 2017.

[63] Jingjing Yang, Hanchen Yu, Jie Yin, Ming Gao, Zemin Wang, and Xiaoyan Zeng. Formation and control of martensite in Ti-6Al-4V alloy produced by selective laser melting. *Materials & Design*, 108:308–318, October 2016.

[64] Haize Galarraga, Robert J. Warren, Diana A. Lados, Ryan R. Dehoff, Michael M. Kirka, and Peeyush Nandwana. Effects of heat treatments on microstructure and properties of Ti-6Al-4V ELI alloy fabricated by electron beam melting (EBM). *Materials Science and Engineering: A*, 685:417–428, February 2017.

[65] M. L. Spaeth, P. J. Wegner, T. I. Suratwala, M. C. Nostrand, J. D. Bude, A. D. Conder, J. A. Folta, J. E. Heebner, L. M. Kegelmeyer, B. J. MacGowan, D. C. Mason, M. J. Matthews, and P. K. Whitman. Optics Recycle Loop Strategy for NIF Operations above UV Laser-Induced Damage Threshold. *Fusion Science and Technology*, 69(1):265–294, February 2016. Publisher: Taylor & Francis _eprint: https://doi.org/10.13182/FST15-119.